

This discussion paper is/has been under review for the journal Climate of the Past (CP).
Please refer to the corresponding final paper in CP if available.

Effects of eustatic sea-level change, ocean dynamics, and iron fertilization on atmospheric $p\text{CO}_2$ and seawater composition over the last 130 000 years

K. Wallmann¹, B. Schneider², and M. Sarnthein^{2,3}

¹GEOMAR Helmholtz Centre for Ocean Research Kiel, Wischhofstr. 1–3, 24148 Kiel, Germany

²Institut für Geowissenschaften, University of Kiel, Olshausenstr. 40, 24098 Kiel, Germany

³Geologisch-Paläontologisches Institut, University of Innsbruck, Innrain 50, 6020 Innsbruck, Austria

Received: 19 May 2015 – Accepted: 31 May 2015 – Published: 29 June 2015

Correspondence to: K. Wallmann (kwallmann@geomar.de)

Published by Copernicus Publications on behalf of the European Geosciences Union.

Effects of eustatic sea-level change, ocean dynamics, and iron fertilization on atmospheric $p\text{CO}_2$

K. Wallmann et al.

Title Page

Abstract

Introduction

Conclusions

References

Tables

Figures

◀

▶

◀

▶

Back

Close

Full Screen / Esc

Printer-friendly Version

Interactive Discussion

Abstract

We developed and employed an earth system model to explore the forcings of atmospheric $p\text{CO}_2$ change and the chemical and isotopic evolution of seawater over the last glacial cycle. Concentrations of dissolved phosphorus, reactive nitrogen, molecular oxygen, dissolved inorganic carbon (DIC), total alkalinity (TA), ^{13}C -DIC and ^{14}C -DIC were calculated for 24 ocean boxes. The bi-directional water fluxes between these model boxes were derived from a 3-D circulation field of the modern ocean (Opa 8.2, NEMO) and tuned such that tracer distributions calculated by the box model were consistent with observational data from the modern ocean. To model the last 130 kyr, we employed records of past changes in sea-level, ocean circulation, and dust deposition. According to the model, about half of the glacial $p\text{CO}_2$ drawdown may be attributed to marine regressions. The glacial sea-level low-stands implied steepened ocean margins, a reduced burial of particulate organic carbon, phosphorus, and neritic carbonate at the margin seafloor, a decline in benthic denitrification, and enhanced weathering of emerged shelf sediments. In turn, they led to a distinct rise in the standing stocks of DIC, TA, and nutrients in the global ocean, promoted the glacial sequestration of atmospheric CO_2 in the ocean, and added ^{13}C - and ^{14}C -depleted DIC to the ocean as recorded in benthic foraminifera signals. The other half of the glacial drop in $p\text{CO}_2$ was linked to reduced deep ocean dynamics, a shoaling of Atlantic meridional overturning circulation, and a rise in iron fertilization. The increased transit time of deep waters in the glacial ocean led to significant ^{14}C depletions with respect to the atmosphere. The deglacial rapid and stepwise rise in atmospheric $p\text{CO}_2$ was induced by upwelling both in the Southern Ocean and subarctic North Pacific and promoted by a drop in dust-borne iron discharge to the Southern Ocean. The deglacial sea-level rise led to a gradual decline in nutrient, DIC, and TA stocks, a slow change due to the large size and extended residence times of dissolved chemical species in the ocean. Thus, the rapid deglacial rise in $p\text{CO}_2$ was dominated by fast changes in ocean dynamics and reduced dust deposition whereas the gradual $p\text{CO}_2$ rise over the Holocene may be

Effects of eustatic sea-level change, ocean dynamics, and iron fertilization on atmospheric $p\text{CO}_2$

K. Wallmann et al.

Title Page

Abstract

Introduction

Conclusions

References

Tables

Figures

◀

▶

◀

▶

Back

Close

Full Screen / Esc

Printer-friendly Version

Interactive Discussion



Effects of eustatic sea-level change, ocean dynamics, and iron fertilization on atmospheric $p\text{CO}_2$

K. Wallmann et al.

Title Page

Abstract

Introduction

Conclusions

References

Tables

Figures

◀

▶

◀

▶

Back

Close

Full Screen / Esc

Printer-friendly Version

Interactive Discussion

hanced by the marine regression and the decrease in shallow margin area since major removal fluxes, that is accumulation of neritic carbonate, benthic denitrification, burial of particulate organic carbon (POC) and phosphorus (P), depend on the size of seafloor area located in shallow waters. Various authors and earth system models considered the glacial decrease in shelf carbonate burial as a major driver of ocean chemistry and atmospheric $p\text{CO}_2$ change (Berger, 1982; Opdyke and Walker, 1992; Brovkin et al., 2012; Ganopolski et al., 1998), since neritic carbonates contribute $\geq 50\%$ to the carbonate accumulation at the global seafloor (Milliman and Droxler, 1996; Kleypas, 1997; Berelson et al., 2007). However, the effects of sea-level change on POC and nutrient cycling are largely ignored in state-of-the-art models even though $> 50\%$ of the global benthic denitrification and burial of marine POC and P occur in shelf and upper slope environments (Bernier, 1982; Bohlen et al., 2012; Wallmann, 2010).

Against this background, our contribution aims to explore and quantify the effects of sea-level change, ocean dynamics and dust deposition on seawater composition and atmospheric $p\text{CO}_2$ over the last glacial cycle. We consider both chemical and isotopic changes in seawater composition and employ isotope data ($\delta^{13}\text{C}$, $\Delta^{14}\text{C}$) to constrain changes in ocean dynamics and deep ocean ventilation. Using a simple earth system model, we show that a significant fraction of the $p\text{CO}_2$ drawdown over the glacial period was possibly induced by the marine regression promoting the expansion of dissolved phosphate, nitrate, and total alkalinity inventories in the glacial ocean whereas the fast deglacial $p\text{CO}_2$ rise was to a large degree driven by rapid changes in ocean dynamics and dust deposition.

2 Model set-up

The atmospheric partial pressure of CO_2 ($p\text{CO}_2$) serves as the key prognostic variable of the new multi-box earth system model presented in this paper. It was calculated considering continental weathering and degassing processes and gas exchange with the surface ocean (Wallmann, 2014). The oceans were represented by 24 boxes

Effects of eustatic sea-level change, ocean dynamics, and iron fertilization on atmospheric $p\text{CO}_2$

K. Wallmann et al.

[Title Page](#)

[Abstract](#)

[Introduction](#)

[Conclusions](#)

[References](#)

[Tables](#)

[Figures](#)

[◀](#)

[▶](#)

[◀](#)

[▶](#)

[Back](#)

[Close](#)

[Full Screen / Esc](#)

[Printer-friendly Version](#)

[Interactive Discussion](#)

(Fig. 2). The major ocean basins North Atlantic (NA, 30–60° N), Tropical Atlantic (TA, 30° N–30° S), Southern Ocean (SO, > 30° S), Tropical Indo-Pacific (TIP, 30° N–30° S), North Pacific (NP, 30–60° N), and Arctic Ocean (AR, > 60° N; including the Greenland-Norwegian Sea) each were divided into surface, intermediate, deep and bottom water boxes extending from 0–100, 100–2000, 2000–4000 to > 4000 m water depth, respectively. The following tracer concentrations were calculated as prognostic variables for each of the water boxes: salinity (Sal), dissolved phosphorus (DP), dissolved reactive nitrogen (DN), dissolved oxygen (DO), total alkalinity (TA), dissolved inorganic carbon (DIC), dissolved inorganic ^{13}C (^{13}C -DIC), and dissolved inorganic radiocarbon (^{14}C -DIC). The set-up of the model is presented in Appendix A. Appendix B explains how sea-level change affects removal fluxes at continental margins and how these effects are considered in the model.

Eustatic sea-level change was applied as major model forcing (Fig. 3). Changes in global ocean volume, salinity, depositional area at continental margins and exposed shelf area were derived from the sea-level record (Stanford et al., 2011; Waelbroeck et al., 2002) and the hypsographic curve (Eakins and Sharman, 2012). The burial rate of neritic carbonates was reduced during marine regressions in proportion to the decrease in seafloor area available for the growth of tropical reefs and carbonate platforms (Appendix B). We tested the degree to which the decrease in seafloor area at 0–100 and 100–2000 m water depth during glacial sea-level low-stands affected benthic denitrification and the burial of organic carbon and marine phosphorus on the continental shelf and slope (Appendix B) while we assumed that carbonate, P, and POC weathering were promoted by the exposure of shelf sediments (Appendix A).

The comprehensive geological data base on benthic foraminiferal $\delta^{13}\text{C}$ (Oliver et al., 2010; Sarnthein et al., 1994) was employed to constrain water fluxes for the LGM. Mean $\delta^{13}\text{C}$ -DIC values were calculated for those ocean boxes where sufficient $\delta^{13}\text{C}$ data were available and compared to model results. The LGM water fluxes were tuned until the model reproduced the $\delta^{13}\text{C}$ distribution pattern (Table A5). The resulting fluxes are shown in Fig. 2. The southward water flux from the Atlantic into the Southern

Effects of eustatic sea-level change, ocean dynamics, and iron fertilization on atmospheric $p\text{CO}_2$

K. Wallmann et al.

Title Page

Abstract

Introduction

Conclusions

References

Tables

Figures



Back

Close

Full Screen / Esc

Printer-friendly Version

Interactive Discussion

Ocean was relocated from deep (2000–4000 m) to intermediate waters (100–2000 m) to mimic the shoaling of the Atlantic Meridional Overturning Circulation (AMOC) which is well documented not only by $\delta^{13}\text{C}$ data but also in various other proxy records (Curry and Oppo, 2005; Piotrowski et al., 2005; Roberts et al., 2010). Bottom water fluxes from the Southern Ocean into the Atlantic were enhanced during the LGM while the northward flow of surface water was reduced. The overall water exchange between Atlantic and Southern Ocean was maintained constant at 15.4 Sv. The bottom and deep water exchange between the Southern Ocean and the Indo-Pacific was reduced by 5 Sv to reproduce the $\delta^{13}\text{C}$ data (Table A5).

The eustatic sea-level curve (Fig. 3a) was applied to change ocean dynamics continuously over time, i.e. to define water fluxes over the full model period (Fig. 4a–c). Thus we assumed that AMOC shoaled gradually during the transition from interglacial to full glacial conditions (130–21 ka) while the horizontal exchange flux of intermediate waters between Southern Ocean and Tropical Indo-Pacific was enhanced over the glacial to mimic the ventilation of tropical OMZs observed in various proxy records (Altabet et al., 1995; Jaccard and Galbraith, 2012). Additional rapid changes were implemented for the deglacial period (Fig. 4a and d). NADW formation was strongly reduced during Heinrich Event 1 (H1) and the Younger Dryas (McManus et al., 2004) while upwelling pulses were prescribed in the Southern Ocean during H1 and the Bølling-Allerød (Anderson et al., 2009; Skinner et al., 2010) and in the North Pacific during H1 (Rae et al., 2014). The differences between $\Delta^{14}\text{C}$ values recorded in benthic and pelagic foraminifera in the deglacial Southern Ocean (Skinner et al., 2010) and North Pacific (Rae et al., 2014) were compared to differences in $\Delta^{14}\text{C}$ -DIC between the corresponding deep water and surface water boxes calculated in the model and the timing and intensity of deglacial mixing events was varied until the model output was consistent with these data. In addition, the deglacial ice-core record of $p\text{CO}_2$ (Marcott et al., 2014) and biogenic opal accumulation rates (Anderson et al., 2009) were employed to constrain the timing and intensity of upwelling pulses in the Southern Ocean. The iron accumulation record from site ODP 1090 was used to constrain changes in nutrient

utilization in the Southern Ocean (Martinez-Garcia et al., 2014) assuming that the increase in iron accumulation observed at this site directly translates into an increase in the efficiency of nutrient utilization (Fig. 4e). To calculate realistic marine isotope trends the changing isotopic compositions of atmospheric CO₂ were set to the values documented in the geological record (Fig. 4f–g).

3 Results and discussion

The model was run over a period of 130 kyr to simulate the behavior of the global system over one full glacial cycle. Simulations start at 130 ka with modern (pre-human) tracer distributions applied as initial values. The standard model run (STD) considers all effects induced by sea-level change, changes in ocean circulation, and iron fertilization, that is the full model forcing as defined in Figures 3 and 4. Additional simulations were performed to better understand the controls on atmospheric pCO₂ and the chemical and isotopic composition of seawater. Simulation STD-CC was run with constant circulation, that is, all water fluxes were maintained at the Holocene level (upper panel of Fig. 2, Table A3) over the full model period, whereas simulation STD-CC-CN was performed with the Holocene circulation field and constant nutrient utilization.

3.1 Atmospheric pCO₂

The pCO₂ trend recorded in ice cores (Monnin et al., 2001, 2004; Marcott et al., 2014; Petit et al., 1999) was well reproduced by the standard simulation (Figs. 5a and 7a). Over the last interglacial, atmospheric pCO₂ increased from an initial value of 280 ppmv at 130 ka to 285 ppmv at 120 ka (Fig. 5a). This increase was accompanied by a decline in nutrient concentrations (Fig. 5f–g) and export production (Fig. 6d), supported by the high sea-level stand promoting burial of phosphorus and benthic denitrification in continental margin sediments. Over the subsequent glacial period, pCO₂ declined due to sea-level fall, iron fertilization, and the decline in deep ocean ventilation un-

Effects of eustatic sea-level change, ocean dynamics, and iron fertilization on atmospheric pCO₂

K. Wallmann et al.

Title Page

Abstract

Introduction

Conclusions

References

Tables

Figures

◀

▶

◀

▶

Back

Close

Full Screen / Esc

Printer-friendly Version

Interactive Discussion

Effects of eustatic sea-level change, ocean dynamics, and iron fertilization on atmospheric $p\text{CO}_2$

K. Wallmann et al.

Title Page

Abstract

Introduction

Conclusions

References

Tables

Figures

◀

▶

◀

▶

Back

Close

Full Screen / Esc

Printer-friendly Version

Interactive Discussion

til 21 ka, when a $p\text{CO}_2$ minimum of 190 ppmv was reached (Fig. 7). The simulated glacial $p\text{CO}_2$ drawdown was discontinuous, marked by several steps and turning points (Fig. 5a). Major minima in atmospheric $p\text{CO}_2$ occurred at 90 ka (220 ppmv) and 65 ka (198 ppmv). Both of them are well documented in the ice-core record (Fig. 5a) and accompanied by maxima in iron fertilization (Fig. 4e) and minima in sea-level (Fig. 3a). Sea-level fall and iron fertilization, thus, may have driven most of the glacial $p\text{CO}_2$ decline. Moreover, they may have induced major turning points in the glacial $p\text{CO}_2$ record.

At constant ocean circulation and nutrient utilization (simulation STD-CC-CN), $p\text{CO}_2$ declined to a LGM value of 234 ppmv (Fig. 5a). Additional simulations based on the standard simulation STD helped us to specify the driving forces for this decline (Table 1). To study their effect on $p\text{CO}_2$ we suppressed the temporal changes of individual variables. A first simulation test was based on the assumption of constant modern sea surface temperatures (SSTs). It showed that the glacial decline in global mean SST by ca. 2°C (Schmittner et al., 2011) induced a $p\text{CO}_2$ decline by 16 ppmv since the solubility of CO_2 in surface waters was enhanced under low temperatures (compare rows 1 and 2 in Table 1). In a second simulation, salinity was set constant, while the other model parameters varied as defined in the STD simulation. Accordingly, the peak glacial increase in salinity induced a relative atmospheric $p\text{CO}_2$ rise by 5 ppmv by lowering the solubility of CO_2 in surface waters (Table 1). In a third test, both salinity and the volume of the ocean boxes were kept constant over time. Changes in these parameters induced an LGM $p\text{CO}_2$ rise by 13 ppmv (Table 1), illustrating that the contraction of the ocean volume during glacial sea-level low-stands reduced the ocean's capacity to sequester atmospheric CO_2 . In summary, the model runs confirmed previous calculations (Broecker, 1982) showing that the net effect of SST, volume, and salinity changes on glacial $p\text{CO}_2$ is small (decrease by 3 ppmv). Thus, other processes need to be invoked to explain the large glacial drawdown of atmospheric CO_2 simulated by model run STD-CC-CN.

Effects of eustatic sea-level change, ocean dynamics, and iron fertilization on atmospheric $p\text{CO}_2$

K. Wallmann et al.

Title Page

Abstract

Introduction

Conclusions

References

Tables

Figures

◀

▶

◀

▶

Back

Close

Full Screen / Esc

Printer-friendly Version

Interactive Discussion

Changes in the flux of dissolved phosphorus (DP) exert large effects on $p\text{CO}_2$, since DP is the ultimate limiting nutrient of the model ocean. Neglecting the glacial increase in the weathering of P-bearing solids is raising the LGM $p\text{CO}_2$ value by 50 ppmv (Table 1, rows 5 vs. 1). In a further simulation we evaluated the overall effect of chemical weathering on atmospheric $p\text{CO}_2$, that is, the weathering rates of P-bearing solids, carbonate, and POC were maintained at their modern values over the entire model period (see STD run with constant rates of chemical weathering, Table 1). The net effect was an LGM $p\text{CO}_2$ rise that did not exceed 3 ppmv with respect to simulation STD, since the CO_2 release by POC weathering largely compensated for the CO_2 loss induced by carbonate and P weathering. Applying very high molar C : P ratios for POM in shelf sediments (ca. 200), it was previously calculated that shelf weathering resulted in a net increase rather than decrease in atmospheric $p\text{CO}_2$ (Ushie and Matsumoto, 2012). However, most of the phosphorus in shelf sediments and riverine particles is not organic but bound in other reactive, inorganic phases such as carbonate-fluoro-apatite (Berner and Rao, 1994) which release DP when exposed to weathering (Ruttenberg, 1992; Ruttenberg and Berner, 1993). The global mean atomic ratio of POC over reactive P in shelf sediments is thus lower than the C : P ratio of marine organic matter (Baturin, 2007; Wallmann, 2010). Hence, the glacial weathering of shelf sediments probably induced a small drop rather than a rise in LGM $p\text{CO}_2$ (Table 1).

By contrast, a stronger effect results from testing the glacial decrease in depositional areas at continental margins, as revealed by a simulation that ignores the glacial decline in P burial and reveals a glacial $p\text{CO}_2$ rise by 73 ppmv (Table 1) with respect to the standard case due to the decline in DP concentration and export production. An additional simulation with constant depositional area for POC burial resulted in a pronounced drawdown of both atmospheric $p\text{CO}_2$ (by 61 ppmv) and DIC since POC burial at continental margins served as major sink for CO_2 and DIC in the model system (Table 1). Changes in the burial of neritic carbonates were mitigated by carbonate compensation at the deep-sea floor and thus had a less drastic effect on atmospheric $p\text{CO}_2$ (change by 10 ppmv, Table 1). Thus the response of the model system to sea-

Effects of eustatic sea-level change, ocean dynamics, and iron fertilization on atmospheric $p\text{CO}_2$

K. Wallmann et al.

[Title Page](#)[Abstract](#)[Introduction](#)[Conclusions](#)[References](#)[Tables](#)[Figures](#)[◀](#)[▶](#)[◀](#)[▶](#)[Back](#)[Close](#)[Full Screen / Esc](#)[Printer-friendly Version](#)[Interactive Discussion](#)

level change was dominated by changes in the burial of P and POC at continental margins. However, the glacial drop in atmospheric $p\text{CO}_2$ that was induced by a decline in P burial, was moderated by a coeval drop in POC burial at continental margins. The overall effect was a strong increase in export production and a transfer of CO_2 from the atmosphere into the ocean via the biological pump. Accordingly, most of the glacial $p\text{CO}_2$ decline in simulation STD-CC-CN was driven by the expansion of the DP inventory and the glacial steepening of ocean margins.

The glacial $p\text{CO}_2$ value dropped by 31 ppmv (from 234 to 203 ppmv) in response to enhanced iron fertilization (difference between simulations STD-CC-CN and STD-CC). This decrease was amplified by the glacial sea-level fall since the nutrient (DP) reservoir that was unlocked by the glacial dust input to the Southern Ocean was expanded as a result of glacial marine regression. The remaining portion of the interglacial-to-peak glacial $p\text{CO}_2$ drop by 13 ppmv down to the final LGM value of 190 ppmv was induced by ocean dynamics (difference between simulation STD and STD-CC). Atmospheric $p\text{CO}_2$ rose by 10 ppmv, when all water fluxes between the Atlantic and the Southern Ocean were maintained at their Holocene level over the entire model period (simulation STD with constant AMOC, Table 1). The glacial AMOC shoaling (Fig. 4a–b) thus contributed 10 ppmv to the LGM decline. This effect can be attributed to enhanced CO_2 storage in the deep Atlantic (> 2000 m water depth) which was less ventilated under glacial conditions, since the formation of northern deep waters was greatly diminished and replaced by southern-source waters enriched in DIC. Thus additional DIC was stored in the glacial deep ocean (Ganopolski et al., 2010; Skinner, 2009; Sarnthein et al., 2013). The glacial decrease in water fluxes between the deep Southern Ocean and Tropical Indo-Pacific (Fig. 2) likewise supports further sequestration and storage of CO_2 in the deep ocean and the glacial drawdown of atmospheric $p\text{CO}_2$. The circulation changes applied to simulate LGM conditions (Fig. 2) led to a reduction in the global water exchange across the 2000 m depth horizon from a modern amount of 45 Sv down to 31 Sv near 21 ka.

Effects of eustatic sea-level change, ocean dynamics, and iron fertilization on atmospheric $p\text{CO}_2$

K. Wallmann et al.

[Title Page](#)[Abstract](#)[Introduction](#)[Conclusions](#)[References](#)[Tables](#)[Figures](#)[◀](#)[▶](#)[◀](#)[▶](#)[Back](#)[Close](#)[Full Screen / Esc](#)[Printer-friendly Version](#)[Interactive Discussion](#)

A stepwise increase in $p\text{CO}_2$ was simulated over the deglaciation (Fig. 7). The first step occurred from 18.5 to 16.3 ka when the simulated $p\text{CO}_2$ rose rapidly from 193 to 220 ppmv. A second step followed at 15.9–14.1 ka with a $p\text{CO}_2$ rise from 222 to 244 ppmv, a third step at 13.0–10.8 ka with a strong increase from 243 to 272 ppmv.

The first step was driven by the rapid drop in dust deposition at the glacial termination (Fig. 4e) and the ventilation of intermediate and deep water masses in the North Pacific during H1 (Fig. 4d). The second and third steps were driven by the Southern Ocean where CO_2 was released into the atmosphere due to the abrupt decline in stratification and the further decrease in dust input (Fig. 4d–e). In major parts of the Southern Ocean these steps coincide with maxima in opal accumulation indicating enhanced upwelling (Anderson et al., 2009). Sea-level change was not uncovered as major driver for the rapid deglacial $p\text{CO}_2$ rise since the long residence times of DP (13 kyr) and TA (77 kyr) inhibit fast inventory changes in the global ocean (Wallmann, 2014). By contrast, the $p\text{CO}_2$ increase over the Holocene (10–0 ka), which is closing the glacial cycle, may have been driven by a high sea-level stand inducing a gradual and slow decline in marine DP and TA inventories.

3.2 Dissolved nutrients and oxygen

The standing stock of DP in the global ocean rose under glacial conditions since P burial was diminished by the decrease in depositional area located at shallow water depths (Fig. 6h) while chemical weathering was promoted by the exposure of shelf sediments (Fig. 6g). Most of the glacial DP rise found in our simulations was induced by the glacial steepening of ocean margins reducing the burial of P in margin sediments (Table 1, Fig. 1, Appendix B). Iron fertilization induced a strong decrease in glacial DP stocks since more DP was taken up by phytoplankton to be drawn down and finally buried in marine sediments (simulations STD-CC vs. STD-CC-CN, Figs. 5f, 6d and h), while the glacial DP stock was largely restored by changes in ocean dynamics (simulations STD vs. STC-CC, Fig. 5f) separating the large nutrient pool in the deep ocean from the surface layer. The spatial distribution of DP in the global ocean reflects

Effects of eustatic sea-level change, ocean dynamics, and iron fertilization on atmospheric $p\text{CO}_2$

K. Wallmann et al.

Title Page

Abstract

Introduction

Conclusions

References

Tables

Figures

◀

▶

◀

▶

Back

Close

Full Screen / Esc

Printer-friendly Version

Interactive Discussion

the export of POM by the biological pump and ocean circulation. The overall pattern, that is a strong vertical gradient between depleted surface waters and enriched deep water masses and a significant horizontal gradient between the deep North Atlantic and North Pacific, was maintained over the glacial cycle (Fig. 8). However, the vertical DP gradient was enhanced over the LGM due to iron fertilization and the decrease in deep ocean ventilation. Reactive P accumulation rates in marine sediments can be used to validate our model results. A global compilation of these data confirmed that P accumulation in shelf sediments decreased drastically under glacial conditions (Tamburini and Föllmi, 2009). The resulting decline in global P burial induced an increase in the glacial DP inventory by 17–40 % (Tamburini and Föllmi, 2009) as predicted by our model. Cd/Ca ratios in LGM sediments from the Atlantic Ocean (Boyle and Keigwin, 1982) and $\delta^{13}\text{C}$ records (Duplessy et al., 1988; Sarnthein et al., 1994; Oliver et al., 2010) suggest a steepening of the vertical DP gradients broadly consistent with our model results.

The dissolved oxygen (DO) content of the global ocean decreased under glacial conditions due to the decline in deep ocean ventilation and increase in export production (Fig. 5h). In contrast, it recovered and peaked over the deglaciation since ocean ventilation was enhanced in the Southern Ocean and the North Pacific. The spatial distribution of DO changed significantly under LGM conditions (Fig. 8). Concentrations declined at > 1500 m water depth due to the decrease in ocean ventilation and increase in export production while glacial cooling induced a small DO rise in surface waters. The DO minimum in intermediate waters of the Indo-Pacific expanded and spread into the deep ocean under glacial conditions. The lowest value was calculated for the intermediate water box of the North Pacific where the DO concentration declined to $69 \mu\text{M}$ at 21 ka. The glacial DO decrease in the deep ocean is consistent with a large data set showing that deep waters below 1500 m water depth were significantly depleted in the LGM over all major ocean basins (Jaccard and Galbraith, 2012). The glacial oxygen depletion in the intermediate Indo-Pacific ($76 \mu\text{M}$ during the LGM vs. $96 \mu\text{M}$ in the modern ocean) seems to be at odds with the geological record which shows that oxy-

Effects of eustatic sea-level change, ocean dynamics, and iron fertilization on atmospheric $p\text{CO}_2$

K. Wallmann et al.

Title Page

Abstract

Introduction

Conclusions

References

Tables

Figures

◀

▶

◀

▶

Back

Close

Full Screen / Esc

Printer-friendly Version

Interactive Discussion

our model runs a significant portion of these trends were driven by sea-level change that controlled the burial of neritic carbonate (Fig. 3d) and POC (Fig. 6e) and the rates of POC and carbonate weathering by shelf exposure, in particular during the build-up of glacial ice sheets (Figs. 3h and 6c). The glacial DIC and TA rise was mitigated by iron fertilization enhancing marine export production and carbon burial (compare simulations STD-CC-CN and STD-CC in Figs. 5 and 6). In turn, it was amplified by the glacial decrease in deep ocean ventilation, a reduced turnover rate that also implied a decrease in marine export production, POC burial and pelagic carbonate accumulation (STD-CC vs. STD). Considering changes in ocean volume by about 3% (Fig. 3b), the increase in DIC over the last glacial (118.5–19.5 ka) translates into a mean DIC increase rate of $1.70 \text{ Tmol yr}^{-1}$. By comparison, the CO_2 uptake from the atmosphere as calculated from the glacial rate of $p\text{CO}_2$ decline amounts to $0.17 \text{ Tmol yr}^{-1}$. Thus, only 10% of the glacial DIC rise was induced by CO_2 uptake from the atmosphere. The glacial demise of neritic carbon pools (carbonate and POC) thus formed a major reason for the DIC rise, while the sequestration of atmospheric CO_2 only was of minor importance for the glacial change in seawater composition. Most of the excess DIC accumulating in the glacial ocean originated from neritic carbonates and sedimentary POC released at the exposed shelves and from riverine DIC which was not buried due to the contraction of depositional areas at ocean margins. The accumulation of DIC and TA in the deep ocean was corroborated by a change in Atlantic deep water chemistry. As outlined above, this LGM ocean basin was filled with corrosive southern-source waters compromising the preservation of carbonates at the deep-sea floor and diminishing the rate of pelagic carbonate burial (Table 1, compare simulation STD with constant AMOC and simulation STD). However, the DIC distribution calculated for the LGM indicates that DIC concentrations increased in all major ocean basins (Fig. 9). In summary, the glacial DIC rise was not limited to single ocean basins but spread over the entire global ocean.

The global mean concentration of carbonate ions (CO_3^{2-}) in the deep ocean (> 2000 m) rose over glacial times in simulation STD due to the decline in neritic car-

Effects of eustatic sea-level change, ocean dynamics, and iron fertilization on atmospheric $p\text{CO}_2$

K. Wallmann et al.

Title Page

Abstract

Introduction

Conclusions

References

Tables

Figures

◀

▶

◀

▶

Back

Close

Full Screen / Esc

Printer-friendly Version

Interactive Discussion

bonate burial and dropped over the deglaciation, at least in part, due to the recovery of neritic carbonate deposition (Fig. 10a). The glacial CO_3^{2-} rise was mitigated by the decline in deep ocean ventilation and increase in ocean productivity promoting the sequestration of CO_2 in the deep ocean. The deglacial minimum at 15.5 ka and the subsequent maximum at 13 ka were related to coeval changes in the accumulation rate of pelagic carbonate (Fig. 6f) which were induced by upwelling pulses in the Southern Ocean (Fig. 4d). The Holocene was marked by a continuous CO_3^{2-} decline probably induced by the high sea-level stand promoting neritic carbonate burial. Interestingly, deep ocean pH and CO_3^{2-} trends diverged during the transition into the LGM (Fig. 10a–b), that is, pH dropped while CO_3^{2-} was maintained at a constant level over this period (30–20 ka). Due to this divergence, the late glacial pH was lower (that is, more acidic) than the modern value, while the CO_3^{2-} concentration exceeded the modern concentration in ocean deep waters. This apparent discrepancy may be explained by the fact that alkalinity and DIC were strongly elevated in late glacial seawater (Fig. 5b and e) thereby enhancing the concentrations of both H^+ and CO_3^{2-} ions with respect to the pre-industrial modern ocean.

We ascribe the strong enrichment of dissolved CO_3^{2-} in glacial surface waters to the decline in atmospheric $p\text{CO}_2$ (Fig. 9). These CO_3^{2-} concentrations exceeded Holocene values down to water depths of 1000 m, likewise at northern high latitudes where deep-water formation transmitted the signature of glacial surface waters into the ocean's interior. The carbonate ion concentration was almost constant over the entire Indo-Pacific at > 1000 m water depth since the strong increase in DIC (Fig. 9) was balanced by a corresponding TA rise. These model results compare well with those of B/Ca ratios in benthic foraminifera which probably record CO_3^{2-} changes in ambient bottom waters (Yu et al., 2008, 2013). The model is consistent with glacial to interglacial changes in deep-sea CO_3^{2-} reconstructed from this proxy (Table C1 in Appendix C). The only deviation occurs at > 4 km water depth in the Atlantic where the model predicts elevated LGM values while the data show a glacial CO_3^{2-} depletion (Table C1), possibly the re-

sult of a strong east-west gradient in bottom water chemistry not resolved yet by the B/Ca data that accordingly may not be fully representative for the Atlantic at large.

The glacial distribution pattern of $\delta^{13}\text{C}$ -DIC values calculated in the standard simulation (Fig. 11) is broadly consistent with observations (Oliver et al., 2010). To avoid circular reasoning, this evidence cannot be used to validate the model results, since glacial $\delta^{13}\text{C}$ -DIC data were employed to define the LGM circulation pattern (Sect. 2, Table A5 in Appendix A). In all simulations global mean $\delta^{13}\text{C}$ -DIC values mirror the DIC concentrations (Fig. 5b–c) and get depleted with rising DIC concentrations, and vice versa. This anti-correlation may be linked to the turnover of POC being strongly depleted in ^{13}C as compared to average seawater. The glacial demise of the sedimentary POC pool, induced by the weathering of exposed shelf sediments and the decline in depositional areas at continental margins, contributed significantly to the glacial DIC rise and determined the isotopic evolution of seawater (Broecker, 1982; Wallmann, 2014). The glacial $\delta^{13}\text{C}$ -DIC depletion was widely ascribed to a glacial loss of terrestrial biomass (Shackleton, 1977; Köhler and Fischer, 2004). However, our model can reproduce almost the entire glacial shift to depleted $\delta^{13}\text{C}$ -DIC values recorded in benthic foraminifera ($0.34 \pm 0.19\%$; Peterson et al., 2014) without invoking net changes in terrestrial biomass (Table A5). This result is consistent with a new modeling study suggesting that the rise in carbon buried in permafrost and under ice largely compensated for the decline in peat, soil and biomass carbon over the LGM (Brovkin and Ganopolski, 2015).

3.4 Radiocarbon

Atmospheric $\Delta^{14}\text{C}$ - CO_2 was forced to follow the IntCal13 values derived from the geological record by varying the ^{14}C -production rate in the atmosphere (Appendix A, Sect. A8). The ^{14}C production rate was calculated for each time step considering the ^{14}C transfer from atmosphere to oceans and changes in the inventories of atmospheric CO_2 and ^{14}C - CO_2 . The difference between global mean $\Delta^{14}\text{C}$ -DIC and atmo-

Effects of eustatic sea-level change, ocean dynamics, and iron fertilization on atmospheric $p\text{CO}_2$

K. Wallmann et al.

Title Page

Abstract

Introduction

Conclusions

References

Tables

Figures

◀

▶

◀

▶

Back

Close

Full Screen / Esc

Printer-friendly Version

Interactive Discussion

Effects of eustatic sea-level change, ocean dynamics, and iron fertilization on atmospheric $p\text{CO}_2$

K. Wallmann et al.

Title Page

Abstract

Introduction

Conclusions

References

Tables

Figures

◀

▶

◀

▶

Back

Close

Full Screen / Esc

Printer-friendly Version

Interactive Discussion

spheric $\Delta^{14}\text{C-CO}_2$ ($\Delta\Delta^{14}\text{C-DIC} = \Delta^{14}\text{C-DIC} - \Delta^{14}\text{C-CO}_2$) depended on the radiocarbon content of the atmosphere (Figs. 5d, 4g, and 12). $\Delta^{14}\text{C-CO}_2$ and the model-derived $\Delta\Delta^{14}\text{C-DIC}$ were anti-correlated, since the ^{14}C uptake from the atmosphere was insufficient to raise the radiocarbon content of the model ocean up to the level of elevated $\Delta^{14}\text{C-CO}_2$ values attained during periods of strong atmospheric radiocarbon production. This anti-correlation was also observed in an additional simulation (Fig. 12b) where the carbon cycle and ocean circulation were maintained at a steady state representing Holocene boundary conditions, whereas $\Delta^{14}\text{C-CO}_2$ values were forced to follow the IntCal13 record. In further steady-state simulations the radiocarbon production rate in the atmosphere was held constant over time while the carbon cycle operated in a Holocene steady-state mode with a constant $p\text{CO}_2$ value of $280 \mu\text{atm}$. These model runs show that the steady-state $\Delta\Delta^{14}\text{C-DIC}$ values attained after about 100 kyr simulation time decreased with increasing production rate (Appendix C, Table C2). As previously shown, changing production rates of radiocarbon in the atmosphere may affect the difference between $\Delta^{14}\text{C}$ values in planktonic and benthic foraminifera (Adkins and Boyle, 1997) and the contrast between atmospheric and marine $\Delta^{14}\text{C}$ values (Franke et al., 2008). However, these effects were regarded as transient features induced by a slow ^{14}C transfer from the atmosphere into the ocean. In contrast, the results of our steady-state model suggest that ^{14}C depletion of the ocean during periods of elevated atmospheric ^{14}C production can be a permanent steady-state feature (Table C2), a conclusion further substantiated by a simple steady-state model presented in Appendix D.

The standard simulation STD yielded a mean ocean $\Delta\Delta^{14}\text{C-DIC}$ of -270‰ for the LGM (21 ka) and -152‰ at 0 ka corresponding to a glacial $\Delta\Delta^{14}\text{C-DIC}$ decline by 118‰ . The simulations depicted in Fig. 12b show that multiple processes contributed to the ^{14}C glacial depletion of the ocean with respect to the atmosphere. These include the glacial decline in deep ocean ventilation, sea-level fall, iron fertilization, and rise in atmospheric radiocarbon production. The $\Delta\Delta^{14}\text{C-DIC}$ decline observed upon sea-level fall in part was induced by the glacial decline in sedimentary carbon pools adding

Effects of eustatic sea-level change, ocean dynamics, and iron fertilization on atmospheric $p\text{CO}_2$

K. Wallmann et al.

[Title Page](#)[Abstract](#)[Introduction](#)[Conclusions](#)[References](#)[Tables](#)[Figures](#)[◀](#)[▶](#)[◀](#)[▶](#)[Back](#)[Close](#)[Full Screen / Esc](#)[Printer-friendly Version](#)[Interactive Discussion](#)

fossil carbon to the global ocean. Glacial changes in ocean circulation contributed to the $\Delta\Delta^{14}\text{C}$ -DIC decline since the glacial demise of ventilation across the 2000 m depth horizon isolated the deep ocean from the atmosphere. However, the simulations suggest that changes in ocean ventilation possibly were responsible for less than one third of the glacial rise in the radiocarbon contrast between global ocean and atmosphere.

Atmospheric ^{14}C production rates calculated in the model showed the same trends for all simulations (Fig. 12c). They attained very high values at 25 ka and declined over time. The only significant difference between the model runs occurred during the deglaciation. The standard simulation yielded elevated production rates for this period since the rapid ventilation of the deep ocean considered in simulation STD drew radiocarbon from the atmosphere such that the production rate was enhanced to maintain atmospheric $\Delta^{14}\text{C}$ - CO_2 at the deglacial level documented by IntCal13 (Fig. 12a). Our model results may support the hypothesis that a significant fraction of the $\Delta^{14}\text{C}$ - CO_2 record is controlled by changes in atmospheric radiocarbon production (Köhler et al., 2006; Broecker et al., 2004). However, in contrast to our model approach various authors have proposed that most of the $\Delta^{14}\text{C}$ - CO_2 record can be explained by changes in glacial ocean dynamics and carbon cycling without invoking significantly elevated rates of atmospheric radiocarbon production (Muscheler et al., 2005; Robinson et al., 2005). The Holocene trends calculated in the model are similar to those observed in the ^{10}Be ice-core record (Muscheler et al., 2005) and derived from Holocene geo-magnetic data (Laj et al., 2002) while the glacial values are closer to the stacked sedimentary ^{10}Be record (Frank et al., 1997). Various reasons have been evoked to explain the deviations between different records of atmospheric radionuclide production (Köhler et al., 2006). The controversy suggests a clear need to develop a better constrained record of atmospheric ^{14}C production suitable for model validations (Fig. 12d).

The spatial distribution of radiocarbon in the global ocean changed significantly during the LGM (Fig. 11). According to the standard simulation $\Delta\Delta^{14}\text{C}$ -DIC values were strongly depleted over the entire ocean and reached a minimum of -356% in North Pacific deep water. Both, vertical and horizontal gradients were strengthened during the

Effects of eustatic sea-level change, ocean dynamics, and iron fertilization on atmospheric $p\text{CO}_2$

K. Wallmann et al.

[Title Page](#)

[Abstract](#)

[Introduction](#)

[Conclusions](#)

[References](#)

[Tables](#)

[Figures](#)

[◀](#)

[▶](#)

[◀](#)

[▶](#)

[Back](#)

[Close](#)

[Full Screen / Esc](#)

[Printer-friendly Version](#)

[Interactive Discussion](#)

LGM. In the modern ocean, marine $\Delta^{14}\text{C}$ -DIC values are correlated with DIC concentrations at water depths below 2000 m (Sarnthein et al., 2013). If this correlation also holds for the glacial ocean, glacial $\Delta\Delta^{14}\text{C}$ -DIC values may be used as proxy for DIC concentrations in glacial seawater (Sarnthein et al., 2013). The model results show that the correlation was indeed maintained in the glacial ocean and the slope of the correlation was similar for all model runs and time slices (Fig. 13). However, the regression line for glacial conditions was shifted to lower DIC and $\Delta\Delta^{14}\text{C}$ -DIC values due to changes in ocean carbon cycling and elevated radiocarbon production rates in the glacial atmosphere. Thus $\Delta\Delta^{14}\text{C}$ -DIC values may serve as new proxy for DIC concentrations in ancient seawater, if suitable methods are found to correct for the glacial shift observed in the simulations (Fig. 13). The overall LGM pattern calculated in the standard simulation (Fig. 11) compares well with trends derived from the radiocarbon contents of planktonic and benthic foraminifera even though radiocarbon data indicate strong gradients within ocean basins, which were not resolved by the box model (Appendix C, Table C3). A recent review of glacial $\Delta\Delta^{14}\text{C}$ -DIC data (Sarnthein et al., 2013) revealed radiocarbon depletions in the deep Atlantic, Southern Ocean and Indo-Pacific broadly consistent with those calculated by the model. However, the model was not able to reproduce very strong radiocarbon depletions measured at some deep water sites due to its coarse spatial resolution (Table C3). Moreover, it predicts significant ^{14}C -depletions in the Atlantic thermocline which are inconsistent with coral ^{14}C data (Robinson et al., 2005). ^{14}C measurements in foraminiferal shells and corals from the glacial ocean feature strong spatial and temporal variability (Broecker et al., 2004; Sarnthein et al., 2013). More data will help to resolve this variability and constrain the radiocarbon distribution and dynamics of the glacial ocean.

4 Conclusions

Since many relevant processes are not fully understood outcomes of earth system models depend on somewhat subjective choices of model parameterizations. Never-

theless, we are confident that the major conclusions drawn from our study are robust, since the structure of our model is based on sound geochemical principals and the model results are consistent with observations in the modern and glacial ocean.

Our model experiments suggest that the glacial sea-level fall induced an expansion of nutrient and alkalinity stocks in the global ocean contributing significantly to the drawdown of atmospheric $p\text{CO}_2$. Most of the glacial decline in global mean $\delta^{13}\text{C-DIC}$ observed in benthic foraminifera can be attributed to the weathering of exposed shelf sediments and the glacial decline in POC burial. Glacial changes in seawater chemistry and atmospheric composition were also affected by iron fertilization and ocean dynamics. Iron fertilization promoted export production in the Southern Ocean and burial of POC, particulate P, and pelagic carbonate at the deep-sea floor. These changes mitigated the expansion of the dissolved nutrient, TA and DIC stocks in the ocean induced by the marine regression. The nutrient and CO_2 concentrations in surface waters of the Southern Ocean were reduced by iron fertilization such that more CO_2 could be retained in the ocean interior. The glacial AMOC shoaling and decline in deep ocean ventilation amplified the rise in dissolved nutrient and carbon stocks in the glacial ocean since export production and burial were restricted by the enclosure of nutrients in the deep ocean. The glacial isolation of the deep ocean contributed to the $p\text{CO}_2$ drawdown since more CO_2 was stored in poorly ventilated deep water masses.

The rapid and stepwise rise in atmospheric $p\text{CO}_2$ over the deglaciation was possibly induced by the repeated break-down of Southern Ocean stratification and the sudden ventilation of intermediate and deep water masses in the North Pacific over Heinrich Event 1. The decrease in dust and iron delivery to the Southern Ocean contributed strongly to the deglacial $p\text{CO}_2$ increase. The deglacial sea-level rise supported the $p\text{CO}_2$ rise and induced a decline in nutrient and carbon stocks in the global ocean. These stocks changed only slowly due to their large size and the extended residence times of chemical species in the global ocean. The gradual $p\text{CO}_2$ rise over the Holocene can be attributed to the slow relaxation of nutrient and carbon stocks promoting CO_2 transfer from the ocean into the atmosphere. The slow relaxation is also

Effects of eustatic sea-level change, ocean dynamics, and iron fertilization on atmospheric $p\text{CO}_2$

K. Wallmann et al.

[Title Page](#)[Abstract](#)[Introduction](#)[Conclusions](#)[References](#)[Tables](#)[Figures](#)[◀](#)[▶](#)[◀](#)[▶](#)[Back](#)[Close](#)[Full Screen / Esc](#)[Printer-friendly Version](#)[Interactive Discussion](#)

Effects of eustatic sea-level change, ocean dynamics, and iron fertilization on atmospheric $p\text{CO}_2$

K. Wallmann et al.

[Title Page](#)[Abstract](#)[Introduction](#)[Conclusions](#)[References](#)[Tables](#)[Figures](#)[◀](#)[▶](#)[◀](#)[▶](#)[Back](#)[Close](#)[Full Screen / Esc](#)[Printer-friendly Version](#)[Interactive Discussion](#)

responsible for the imbalance in phosphate and TA sources and sinks observed in the pre-human modern ocean (Wallmann, 2010, 2014). Stocks of these chemical species are declining until today since tens of thousands of years are needed to draw down the dissolved P and TA inventories from their peak values attained over the last glacial maximum.

Various earth system models were previously used to study potential controls of past changes in atmospheric $p\text{CO}_2$ over the last glacial cycle. All models show changes that resulted from several interacting forcings including ocean dynamics and iron fertilization (Köhler et al., 2005, 2006; Ganopolski et al., 2010; Brovkin et al., 2012). The major new component of the present model is linked to the simulation of POM and nutrient cycling at continental margins under eustatic sea-level change (as explained in detail in Appendix B). The changing turnover of sedimentary POC, N and P has a strong effect on seawater chemistry and may have contributed significantly to the glacial drawdown and Holocene rise of atmospheric $p\text{CO}_2$. It should, thus, be considered in future earth system models.

According to standard Milankovitch theory (Milankovitch, 1941), variations in summer insolation at high latitudes (Berger and Loutre, 1991) cause waxing and waning of northern ice sheets (Fig. 14). Most of the global climate change over a glacial cycle is thus believed to be driven by northern summer insolation and ice sheet dynamics (Denton et al., 2010). However, it has always been difficult to explain why atmospheric $p\text{CO}_2$ declined over glacial periods and how this drop was connected to the built-up of large continental ice sheets. The sea-level effects explored in this paper provide the missing link between glacial ice sheet and $p\text{CO}_2$ dynamics. The sea-level-driven $p\text{CO}_2$ decline was amplified by a decrease in deep ocean ventilation, a decline in sea surface temperature, and enhanced dust deposition. These additional changes were driven by a combination of greenhouse gas, albedo, and insolation forcing (Fig. 14). Glacial terminations occurred when summer insolation increased at northern latitudes (Raymo et al., 1997), ice sheets reached a critical size (Denton et al., 2010), and carbonate compensation at the deep-sea floor reversed the declining $p\text{CO}_2$ trend (Wallmann,

Effects of eustatic sea-level change, ocean dynamics, and iron fertilization on atmospheric $p\text{CO}_2$

K. Wallmann et al.

Title Page

Abstract

Introduction

Conclusions

References

Tables

Figures

◀

▶

◀

▶

Back

Close

Full Screen / Esc

Printer-friendly Version

Interactive Discussion

2014). The deglacial warming was again driven by greenhouse gas, albedo, and insolation forcing promoting the retreat of continental ice sheets, sea-level rise, ocean ventilation, and the decline in dust deposition in a positive feedback mode.

Due to their internal non-linear dynamics, continental ice sheets are able to generate 100 kyr cycles with a slow glacial expansion and rapid deglacial contraction of ice volume under Milankovitch forcing even though insolation oscillates on much shorter time scales (Imbrie and Imbrie, 1980; Abe-Ouchi et al., 2013; Ganopolski and Calov, 2011; Pollard, 1983). Positive feedbacks embedded in the global carbon cycle are able to generate a 100 kyr cycle without any form of external forcing when surface temperature, ice volume and sea-level are assumed to be controlled by $p\text{CO}_2$ (Wallmann, 2014). Thus, both, continental ice sheets and the global carbon system have the inherent tendency to generate cycles with a length of 100 kyr. They interact via sea-level and $p\text{CO}_2$ change, respond to insolation forcing, control changes in the climate system (surface temperature, ocean and atmospheric circulation, dust deposition) and may generate the 100 kyr cycle dominating late Quaternary climate change.

Appendix A: Model set-up and calibration

A1 Data and procedures for model calibration

Mean tracer concentrations were calculated for each of the model boxes using the GLODAP data base for total alkalinity, DIC, ^{13}C -DIC and ^{14}C -DIC (Key et al., 2004) and the World Ocean Atlas (WOA01) for temperature, salinity, PO_4 , NO_3 and O_2 (Conkright et al., 2002). ^{14}C -DIC-data were corrected by subtracting the bomb- ^{14}C signal and DIC data were corrected for the intrusion of anthropogenic CO_2 (Key et al., 2004) whereas ^{13}C -DIC data were not corrected and are thus affected by ^{13}C -depleted anthropogenic CO_2 . The model was run into steady state under pre-anthropogenic boundary conditions and resulting tracer concentrations were compared to data to validate the model output and calibrate the model (Tables A1 and A2). The $p\text{CO}_2$ value and global export

Effects of eustatic sea-level change, ocean dynamics, and iron fertilization on atmospheric $p\text{CO}_2$

K. Wallmann et al.

[Title Page](#)
[Abstract](#)
[Introduction](#)
[Conclusions](#)
[References](#)
[Tables](#)
[Figures](#)
[◀](#)
[▶](#)
[◀](#)
[▶](#)
[Back](#)
[Close](#)
[Full Screen / Esc](#)
[Printer-friendly Version](#)
[Interactive Discussion](#)


production of particulate organic carbon were used as additional constraints, i.e. the calculated values had to comply with the corresponding observations (ca. 280 μm and ca. 700–900 Tmol yr^{-1} , respectively; Sarmiento and Gruber, 2006). For these initial model runs, the riverine fluxes to the ocean were enhanced to compensate for the removal fluxes observed in the modern ocean. The atmospheric $p\text{CO}_2$ value was calculated applying a constant continental CO_2 uptake rate balancing the CO_2 being produced in the modern ocean by carbonate burial and degassing processes (Wallmann, 2014). The isotopic composition of atmospheric CO_2 was maintained at a constant level representative for the pre-human atmosphere ($\delta^{13}\text{C} = -6.5\text{‰}$, $\Delta^{14}\text{C} = 0\text{‰}$). Water fluxes (Table A3) and parameter values for key biogeochemical processes (Table A4) were varied until $p\text{CO}_2$, global export production, and the tracer distribution fields generated by the steady-state box model were consistent with data (Tables A1 and A2). A good fit was obtained for all tracers except ^{13}C -DIC. Most of the ^{13}C mismatch was induced by anthropogenic ^{13}C which has a strong effect on the observations in the modern ocean but was not considered in the model simulations.

A2 Ocean circulation and tracer transport

Water fluxes between adjacent boxes were calculated using output of the Opa 8.2 ocean circulation model in the framework of NEMO (Nucleus for European Modeling of the Ocean) to start with a configuration that is dynamically consistent with a 3-D forward ocean model (Madec et al., 1998). NEMO was forced by atmospheric reanalysis data as described in (Aumont and Bopp, 2006). A more detailed analysis of the resulting large-scale circulation pattern is given in (Bordelon-Katrynski and Schneider, 2012). The calculation of water exchange was based on horizontal and vertical velocities on the box model grid. In order to consider two-way exchange between the boxes, not only the net transports, but fluxes in both directions (northward/southward, up/down) were taken into account. Water fluxes at the atmosphere-ocean boundary were calculated as residual fluxes balancing the water exchange for each vertical column. Test runs with the box model revealed, however, that tracer distributions calculated with the NEMO -

derived water fluxes were inconsistent with tracer data when the NEMO circulation field was applied in the box model. This mismatch was induced by the coarse spatial resolution of the box model and by errors inherent to the NEMO simulations. The NEMO-derived circulation field was, thus, modified to allow for a better fit to the independent observations listed in Tables A1 and A2 and to bring the circulation field in line with other observations and GCM modeling results. Thus, NEMO features a North Atlantic Deep Water (NADW) formation rate of only ca. 10 Sv whereas tracer data (radiocarbon, phosphate, oxygen) constrain this rate at ca. 15 Sv (Broecker et al., 1998). Moreover, NEMO predicts that Antarctic Bottom Water (AABW) up-wells in the Indo-Pacific all the way to the thermocline and surface ocean. This pattern is consistent with the “great ocean conveyor” (Broecker, 1991) but in conflict with other more recent ocean models suggesting that deep water ascent occurs in the Southern Ocean rather than in the Indo-Pacific (Sarmiento and Gruber, 2006). These models show that AABW flowing into the Indo-Pacific returns as deep water to the Southern Ocean where it ascends to form intermediate water masses flowing northwards into the major ocean basins (Imbrie et al., 1993; Gnanadesekian and Hallberg, 2002; Marinov et al., 2006). NEMO also predicts an extremely high rate of vertical water exchange in the Southern Ocean across 2000 m water depth of more than 200 Sv. These strong upward and downward water fluxes are inconsistent with tracer observations showing strong vertical gradients between the deep ocean (> 2000 m water depth) and the overlying water masses. The water fluxes derived from NEMO were modified to remove these biases and to provide more realistic water fluxes for the box model (Table A3). The corresponding best-fit water fluxes are bidirectional, i.e. water flows in both directions between each of the adjacent model boxes (Table A3). The net fluxes (Table A3) were calculated as difference between these opposing fluxes. They represent the meridional overturning circulation (MOC) as implemented in the box model (Fig. 2): NADW is formed in the North Atlantic and Arctic basins at an overall rate of ca. 15 Sv. It flows towards the Southern Ocean where Antarctic Bottom Water (AABW) is formed at a rate of ca. 18 Sv. A minor AABW fraction flows northwards into the Atlantic while most of the AABW is filling the deep

CPD

11, 2405–2481, 2015

Effects of eustatic sea-level change, ocean dynamics, and iron fertilization on atmospheric $p\text{CO}_2$

K. Wallmann et al.

[Title Page](#)

[Abstract](#)

[Introduction](#)

[Conclusions](#)

[References](#)

[Tables](#)

[Figures](#)



[Back](#)

[Close](#)

[Full Screen / Esc](#)

[Printer-friendly Version](#)

[Interactive Discussion](#)

Effects of eustatic sea-level change, ocean dynamics, and iron fertilization on atmospheric $p\text{CO}_2$

K. Wallmann et al.

Title Page

Abstract

Introduction

Conclusions

References

Tables

Figures

◀

▶

◀

▶

Back

Close

Full Screen / Esc

Printer-friendly Version

Interactive Discussion

basins of the Indo-Pacific at a rate of ca. 16 Sv where it up-wells and returns into the Southern Ocean as deep water. Intermediate water formed by deep water ascent in the Southern Ocean flows into the Indo-Pacific at a rate of ca. 14 Sv where it up-wells to form surface water flowing back towards the Southern Ocean. Surface waters flowing northward into the Atlantic and returning as NADW to the Southern Ocean are closing the loop. This overall MOC pattern and the corresponding flow rates are consistent with tracer data and other observations (Sarmiento and Gruber, 2006).

The exchange fluxes between adjacent boxes reflect, both, opposing water flows across the box boundaries and eddy diffusive mixing (Table A3). The large vertical exchange flux between tropical surface and intermediate waters in the Indo-Pacific is thus supported by intense Ekman driven up-welling and down-welling while wind-driven eddy diffusive mixing explains most of the vertical exchange between surface and intermediate water boxes in the North Atlantic, Southern Ocean and North Pacific. The overall vertical water exchange across the 100 m water depth horizon (ca. 297 Sv, Table A3) is sufficiently high to ventilate the global thermocline and to support a global rate of new and export production in the order of 700–900 Tmol yr⁻¹. About 37 % of this vertical exchange flux occurs in the Southern Ocean (> 30° S). The global bidirectional water flux across the 2000 m water depth level is much lower (only 45 Sv, 44 % in the Southern Ocean) while the flux across the 4000 m line amounts to ca. 179 Sv with a 74 % contribution by the Southern Ocean. The box model's major internal boundary for vertical exchange is thus located at 2000 m water depth between the thermocline and the underlying deep ocean.

In box modeling, water fluxes (F_{Wab}) are multiplied by tracer concentrations (C_j) to calculate tracer fluxes (F_{Tab}) between adjacent boxes:

$$F_{\text{Tab}} = C_a \cdot F_{\text{Wab}} \quad (\text{A1})$$

where F_{Wab} and F_{Tab} are the water and tracer fluxes from box a to box b while C_a is the concentration of the considered tracer in box a . The back fluxes from box b to box a

are defined correspondingly:

$$F_{Tba} = C_b \cdot F_{Wba} \quad (A2)$$

Tracer fluxes arising from the water exchange fluxes listed in Table A3 (F_{Wex}) are thus proportional to the concentration difference between adjacent boxes:

$$F_{Tex} = (C_a - C_b) \cdot F_{Wex} \quad (A3)$$

These fluxes can be regarded as diffusion-analog mass transfer processes since their magnitude is proportional to concentration differences rather than concentrations. In contrast, the tracer fluxes arising from the net water fluxes in Table A3 are purely advective. Most box models apply unidirectional advective fluxes, only, and ignore diffusive bidirectional fluxes. Tracer distributions observed in the global ocean and simulated with general circulation models are, however, strongly affected by diffusive processes. With the inclusion of bidirectional fluxes in our box model set-up, we aim to better mimic this diffusive behavior.

The low spatial resolution of box models is problematic and may induce significant errors. For the box model set-up presented in this paper, the largest errors are associated with the upward fluxes from the thermocline into the surface ocean. Tracer concentrations calculated for the intermediate water boxes represent mean values averaged over the depth range 100–2000 m where strong vertical gradients exist in the natural system. Due to these strong vertical gradients, the mean concentration values are not representative for the thermocline waters ascending across the 100 m water depth line. The standard box model approach where tracer fluxes are calculated applying the mean concentration in the source box (s. equations above) was, thus, abandoned for these specific fluxes and tracer fluxes were calculated as:

$$F_{TIS} = C_{TH} \cdot F_{WIS} \quad (A4)$$

where F_{TIS} is the tracer flux from the intermediate water box to the overlying surface water box, F_{WIS} is the corresponding water flux, and C_{TH} is the tracer concentration in

Effects of eustatic sea-level change, ocean dynamics, and iron fertilization on atmospheric pCO_2

K. Wallmann et al.

Title Page

Abstract

Introduction

Conclusions

References

Tables

Figures

◀

▶

◀

▶

Back

Close

Full Screen / Esc

Printer-friendly Version

Interactive Discussion



Effects of eustatic sea-level change, ocean dynamics, and iron fertilization on atmospheric $p\text{CO}_2$

K. Wallmann et al.

[Title Page](#)[Abstract](#)[Introduction](#)[Conclusions](#)[References](#)[Tables](#)[Figures](#)[◀](#)[▶](#)[◀](#)[▶](#)[Back](#)[Close](#)[Full Screen / Esc](#)[Printer-friendly Version](#)[Interactive Discussion](#)

These simulations showed, however, that unrealistically high freshwater fluxes were needed to reproduce the low salinity values observed in the Arctic Ocean surface water box. This problem arises since the standard box model procedure demands that water masses leaving the Arctic carry a chemical signature corresponding to the mean salinity value integrated over the entire Arctic surface ocean. Observations show, however, that Arctic surface waters sinking into the abyss are more salty than mean Arctic surface water. The standard model procedure was, hence, modified to consider this characteristic feature of deep water formation and to avoid unrealistically high freshwater fluxes to the Arctic surface ocean, i.e. an enhanced salinity (+0.9 PSU with respect to the mean salinity of Arctic surface water) was ascribed to the waters sinking into the underlying intermediate water box.

Over a glacial cycle, surface temperatures are regulated by changes in, both, albedo and the partial pressure of greenhouse gases. In the model it was assumed that 50 % of the temperature change is proportional to the prescribed sea-level, i.e. continental ice sheet formation and albedo change while the remaining 50 % are proportional to the logarithm of atmospheric $p\text{CO}_2$ calculated as prognostic model variable. The global mean atmospheric surface temperature was assumed to fall by 3 °C during the glacial while the average sea surface temperature (SST) was allowed to drop by ca. 2 °C (Schmittner et al., 2011). The SST drop was assumed to be twice as high as the global mean at high latitudes and only half as high in the low latitude surface water boxes. Temperatures in intermediate and deep waters were maintained at their modern values, for simplicity.

A4 Phosphorus

The model includes a comprehensive phosphorus cycle. Rivers transport dissolved phosphorus (DP) into the ocean where it is taken up by phytoplankton, gets exported, degraded, buried in marine sediments, and removed via hydrothermal activity (Wallmann, 2014). Export production (F_{EPOP}) of particulate organic P (POP) from the individual surface water boxes across 100 m water depth was calculated applying Liebig's

2014). The rate of silicate weathering was set to a constant value since the weathering of exposed shelf sediments was assumed to compensate for the glacial decrease in silicate weathering in the continental hinterland (Munhoven, 2002). The rate of carbonate weathering was assumed to depend on surface temperature, run-off, and the size of the exposed shelf area (Wallmann, 2014).

A8 Carbon isotopes

The model includes ^{13}C -DIC and ^{14}C -DIC as tracers in addition to total DIC. Isotope ratios as well as $\delta^{13}\text{C}$ and $\Delta^{14}\text{C}$ values of DIC were calculated from ^{13}C -DIC/DIC and ^{14}C -DIC/DIC mole fractions. The gas exchange of ^{13}C - CO_2 across the seawater/atmosphere boundary layer ($F_{13\text{CO}_2}$) was calculated as (Schmittner et al., 2013; Zhang et al., 1995):

$$F_{13\text{CO}_2} = k_W \cdot A_{\text{SUR}} \cdot \alpha_{\text{aq-g}} \cdot \alpha_k \cdot \left(\frac{R_{13\text{DIC}}}{\alpha_{\text{DIC-g}}} \cdot \text{CO}_{2\text{S}} - R_{13\text{CO}_2\text{A}} \cdot \text{CO}_{2\text{SEQ}} \right) \quad (\text{A11})$$

where $\alpha_{\text{aq-g}}$ is the equilibrium fractionation factor for CO_2 gas exchange between seawater and air, α_k is the corresponding kinetic fractionation factor, $\alpha_{\text{DIC-g}}$ is the equilibrium fractionation factor defining the ^{13}C fractionation between DIC and gaseous CO_2 , $R_{13\text{DIC}}$ is the $^{13}\text{C}/^{12}\text{C}$ ratio in DIC, and $R_{13\text{CO}_2\text{A}}$ is the $^{13}\text{C}/^{12}\text{C}$ ratio in atmospheric CO_2 . The isotopic composition of DIC species (CO_2 , HCO_3^- , CO_3^{2-}) was calculated using equilibrium fractionation factors given in (Zeebe and Wolf-Gladrow, 2001). These values were applied to calculate the isotopic composition of exported POC and neritic and pelagic carbonates applying isotopic fractionation factors according to (Ridgeway, 2001) and (Romanek et al., 1992), respectively.

The $^{14}\text{C}/^{12}\text{C}$ fractionation between DIC, CO_2 , POC and CaCO_3 was calculated using the squared ^{13}C equilibrium fractionation factors since the mass difference between ^{14}C and ^{12}C exceeds the $^{13}\text{C} - ^{12}\text{C}$ difference by a factor of 2. The gas exchange of $^{14}\text{C} - \text{CO}_2$ across the seawater/atmosphere boundary layer ($F_{14\text{CO}_2}$) was thus calculated

Effects of eustatic sea-level change, ocean dynamics, and iron fertilization on atmospheric $p\text{CO}_2$

K. Wallmann et al.

Title Page

Abstract

Introduction

Conclusions

References

Tables

Figures

◀

▶

◀

▶

Back

Close

Full Screen / Esc

Printer-friendly Version

Interactive Discussion



as:

$$F_{14\text{CO}_2} = k_W \cdot A_{\text{SUR}} \cdot \alpha_{\text{aq-g}}^2 \cdot \alpha_k \cdot \left(\frac{R_{14\text{DIC}}}{\alpha_{\text{DIC-g}}^2} \cdot \text{CO}_{2\text{S}} - R_{14\text{CO}_2\text{A}} \cdot \text{CO}_{2\text{SEQ}} \right) \quad (\text{A12})$$

where $R_{14\text{DIC}}$ is the $^{14}\text{C}/^{12}\text{C}$ ratio in DIC of the considered surface water box and $R_{14\text{CO}_2\text{A}}$ the $^{14}\text{C}/^{12}\text{C}$ ratio in atmospheric CO_2 . Moreover, ^{14}C -DIC was subject to radioactive decay with a decay constant of $\lambda = 1/8267 \text{ yr}^{-1}$.

$\Delta^{14}\text{C}$ -DIC values were calculated as:

$$\Delta^{14}\text{C} - \text{DIC} = \left(\frac{f_N \cdot \Phi_{14\text{DIC}}}{\Phi_{\text{abs}}} - 1 \right) \cdot 1000 \quad (\text{A13})$$

where $\Phi_{14\text{DIC}}$ is the ^{14}C mole fraction ($\Phi_{14\text{DIC}} = ^{14}\text{C-DIC}/\text{DIC}$), Φ_{abs} is the ^{14}C mole fraction of the standard (1.175×10^{-12} (Mook and Plicht, 1999), pre-human atmosphere with a $\delta^{13}\text{C}$ value of -25‰), f_N is the normalization factor defined as:

$$f_N = \left(\frac{0.975}{\left(1 + \frac{\delta^{13}\text{C}}{1000}\right)} \right)^2 \quad (\text{A14})$$

and $\delta^{13}\text{C}$ is the $\delta^{13}\text{C}$ value of DIC in the considered box in ‰ PDB. The isotopic fractionation experienced by the considered DIC pool was thus taken into account in the calculation of marine $\Delta^{14}\text{C}$ -DIC values by applying the $\delta^{13}\text{C}$ -DIC calculated for the considered ocean box (Stuiver and Polach, 1977).

The isotopic compositions of atmospheric CO_2 were not calculated as prognostic model variables but prescribed using data from the geological record. Ice-core data were applied to define the $\delta^{13}\text{C}$ - CO_2 values (Schmitt et al., 2012) while $\Delta^{14}\text{C}$ - CO_2 values were forced to follow the IntCal13 values (Reimer et al., 2013). The time-dependent radiocarbon production rate (R_{14}) was calculated applying the following equation:

$$R_{14} = k_{14} (\Delta^{14}\text{C-CO}_2(\text{data}) - \Delta^{14}\text{C-CO}_2(\text{model})) \quad (\text{A15})$$

2437

Effects of eustatic sea-level change, ocean dynamics, and iron fertilization on atmospheric $p\text{CO}_2$

K. Wallmann et al.

Title Page

Abstract

Introduction

Conclusions

References

Tables

Figures

◀

▶

◀

▶

Back

Close

Full Screen / Esc

Printer-friendly Version

Interactive Discussion



Effects of eustatic sea-level change, ocean dynamics, and iron fertilization on atmospheric $p\text{CO}_2$

K. Wallmann et al.

Title Page

Abstract

Introduction

Conclusions

References

Tables

Figures

◀

▶

◀

▶

Back

Close

Full Screen / Esc

Printer-friendly Version

Interactive Discussion

where k_{14} is a constant ($\geq 10^5 \text{ mmol yr}^{-1} \text{‰}^{-1}$), $\Delta^{14}\text{C-CO}_2$ (model) is the atmospheric value calculated for each time step of the model, and $\Delta^{14}\text{C-CO}_2$ (data) is the data trend reconstructed from the geological record (Reimer et al., 2013). R_{14} thus increased when $\Delta^{14}\text{C-CO}_2$ (model) was smaller than $\Delta^{14}\text{C-CO}_2$ (data) and vice versa. With this approach, the production rate was varied such that the model always complied with the atmospheric ^{14}C record. The atmospheric radiocarbon model considered production and the decay of radiocarbon in the atmosphere as well as exchange processes with the continents and the surface ocean (Eq. A12). The major output of the atmospheric ^{14}C model was the time-dependent ^{14}C production rate (Eq. A15).

Appendix B: Impact of sea-level change on benthic processes at continental margins

The overwhelming portion of POC produced in the euphotic zone is degraded in the water column before it can reach the seabed. Hence, in the open ocean, only ca. 1 % of the primary production reaches the deep-sea floor (Suess, 1980; Jahnke, 1996; Seiter et al., 2005; Dunne et al., 2007). However, the fraction reaching the seabed increases drastically at continental margins where shallow water depths limit the transit time of POC sinking through the water column. Global models and observations thus indicate that ca. 30 % of ambient primary production reaches the shallow seafloor at 0–50 m water depth (Dunne et al., 2007). Due to this effect and the high productivity of continental margins, the margin seabed located at < 2 km water depths receives ca. $85 \pm 15\%$ of the global POC rain rate (Dunne et al., 2007; Burdige, 2007) even though only 16 % of the global seabed is located at < 2 km water depth (Eakins and Sharman, 2012). Continental margins are even more dominant in terms of POC burial because burial is promoted by the deposition of riverine particles (Berner, 1982, 2004) accumulating mostly on the continental shelf during interglacial sea-level high-stands

(Burwicz et al., 2011). Thus, $90 \pm 10\%$ of the global POC burial takes place at < 2 km water depth (Dunne et al., 2007; Burdige, 2007; Wallmann et al., 2012).

POC rain and burial rates at continental margins declined during glacial sea-level low-stands since the oceans retreated into steeper terrains. During the LGM when the sea-level was 120 m lower than today, the shelf seafloor area at 0–100 m contracted by 73 % while the outer shelf and upper slope area located at 100–2000 m water depth was reduced by 13 % (Eakins and Sharman, 2012) neglecting isostatic adjustment. Considering the high rain rates at shallow water depths (Dunne et al., 2007), the glacial margin contraction diminished the global POC rain rate by possibly up to 50 %. The burial rate of marine POC may have been reduced by a similar proportion since POC burial is ultimately limited by the amount of POC reaching the seabed. However, there are a number of additional factors that affect the rate of POC burial. These include bulk sedimentation rate (Bernier, 1982), surface area of sediment particles (Mayer et al., 2004), oxygen exposure time (Hartnett et al., 1998), and the re-suspension and down-slope transport of shelf POC promoting POC burial at the upper slope (Walsh et al., 1981; Dale et al., 2015). These secondary processes control the burial efficiency of POC, that is the ratio between POC burial and POC rain rate.

POC burial efficiency is to a large degree controlled by sedimentation processes on the shelf that are strongly affected by sea-level change. At high sea-level most of the riverine particle load is deposited on the shelf (Burwicz et al., 2011) while low sea-level stands promote down-slope transport (Hay and Southam, 1977). Hence, data on Quaternary shelf and deep-sea fan sedimentation clearly show that the riverine particle flux was discharged over the shelf edge onto deep-sea fans and abyssal plains by turbidity currents over most of the glacial period (Hay and Southam, 1977; Hay, 1994; Schlünz et al., 1999). The corresponding increase in sedimentation rate probably led to a rise in burial efficiency and POC burial at > 2 km water depths (Burwicz et al., 2011; Wallmann, 2014). The efficiency of POC burial at the continental rise and deep-sea floor may have been further amplified by the glacial decline in dissolved oxygen concentrations in the deep ocean (Jaccard and Galbraith, 2012) favoring the preservation of POC

Effects of eustatic sea-level change, ocean dynamics, and iron fertilization on atmospheric $p\text{CO}_2$

K. Wallmann et al.

Title Page

Abstract

Introduction

Conclusions

References

Tables

Figures

◀

▶

◀

▶

Back

Close

Full Screen / Esc

Printer-friendly Version

Interactive Discussion

Effects of eustatic sea-level change, ocean dynamics, and iron fertilization on atmospheric $p\text{CO}_2$

K. Wallmann et al.

[Title Page](#)

[Abstract](#)

[Introduction](#)

[Conclusions](#)

[References](#)

[Tables](#)

[Figures](#)

[◀](#)

[▶](#)

[◀](#)

[▶](#)

[Back](#)

[Close](#)

[Full Screen / Esc](#)

[Printer-friendly Version](#)

[Interactive Discussion](#)

0–50 m water depth (A_{NM}) which is controlled by sea-level change, only (see Fig. 3). Burial of marine POC and phosphorus (P) at continental margins was assumed to be proportional to POC export production (F_{EPOC}) and the depositional areas at 0–100 m (A_{S}) and 100–2000 m (A_{I}) that were controlled by sea-level change (Fig. 3). The decline in seafloor area at 0–2000 m water depths was applied to parameterize the rise in POC burial at the deep-sea floor induced by the glacial marine regression. We thus effectively assumed that the burial efficiency of POC remained constant at < 2 km water depth but increased at > 2 km during glacial sea-level low-stands.

Phosphorus considered in the model refers to the sum of organic and inorganic P. The latter fraction contributes strongly to P burial since most of the sedimentary organic P is degraded and transformed into inorganic authigenic phases during early diagenesis (Ruttenberg and Berner, 1993). P burial decreases when the dissolved oxygen content of ambient bottom waters (DO) falls below a threshold value of about 20 μM (Wallmann, 2010). This effect was considered by introducing corresponding Monod terms in the P burial flux definitions (Table B2). Benthic denitrification was calculated from the POC rain rate and ambient dissolved oxygen and nitrate concentrations (DN) applying an empirical transfer function calibrated by in situ benthic flux data (Bohlen et al., 2012). The rain rates needed for this function were derived from POC burial rates using the corresponding burial efficiencies. Marine PON burial was calculated from POC burial applying a molar PON/POC ratio of 17/123 (Körtzinger et al., 2001).

The applied parameter values were constrained by field data from the modern ocean (Table B1). The available POC and P burial data suggest that burial is rather evenly distributed between 0–100 and 100–2000 m water depths (Table B1) whereas POM rain rates at 0–100 m clearly exceed the corresponding rates at 100–2000 m (Dunne et al., 2007). This difference is caused by bottom currents transporting marine POM from the inner shelf towards outer shelf and upper slope environments (Walsh et al., 1981). The burial efficiency applied in the model is low at shallow water depth since winnowing by bottom currents affects large parts of the shallow seafloor such that about 70 % of the modern shelf sediments are non-accumulating, relict sands with very low POC

Effects of eustatic sea-level change, ocean dynamics, and iron fertilization on atmospheric $p\text{CO}_2$

K. Wallmann et al.

Title Page

Abstract

Introduction

Conclusions

References

Tables

Figures

◀

▶

◀

▶

Back

Close

Full Screen / Esc

Printer-friendly Version

Interactive Discussion

contents (Burdige, 2007). POM exported laterally from these shallow areas provides POM for slope deposits (Walsh et al., 1981). The highest burial efficiency is applied at 100–2000 m water depth where the deposition of fine-grained riverine particles and low oxygen values in ambient bottom waters favor the preservation of marine POC.

Parameter values and fluxes listed in Tables B1 and B2 refer to global fluxes. These fluxes were distributed among the 6 ocean basins defined in the box model considering the respective seafloor areas and export productions. Neritic carbonate burial was distributed between the Tropical Indo-Pacific and Atlantic (Kleypas, 1997).

The model predicts that the global burial rates of POC and P would decline to 7.9 and $0.14 \text{ Tmol yr}^{-1}$ during the LGM, respectively, if export production and oxygen concentrations were maintained at their modern value. The export production was, however, promoted by the decline in P burial such that the best fit simulation STD produced LGM burial rates of 9.6 and $0.165 \text{ Tmol yr}^{-1}$ compared to modern global rates of 11.5 and $0.18 \text{ Tmol yr}^{-1}$, respectively (s. Table B1).

According to the model, the glacial marine regression affected the chemical and isotopic composition of seawater and the CO_2 content of the atmosphere via a chain of interconnected processes: ocean margins retreated into steeper terrain and shelf areas were exposed by the marine regression; the burial of phosphorus and neritic carbonate and benthic denitrification declined due to the steepening of ocean margins; carbonate, POC, and P weathering rates increased due to the exposure of shelf sediments; atmospheric CO_2 was consumed and converted into dissolved alkalinity by enhanced carbonate weathering while isotopically depleted CO_2 was released into the atmosphere by POC weathering; standing stocks of dissolved nutrients and alkalinity in the ocean expanded due to the decrease in burial and denitrification and the increase in weathering; export production rose due to the increase in the dissolved nutrient stocks and CO_2 was transferred from the atmosphere into the ocean interior by the intensified biological pump while CO_2 sequestration was supported by enhanced seawater alkalinity.

Effects of eustatic sea-level change, ocean dynamics, and iron fertilization on atmospheric $p\text{CO}_2$

K. Wallmann et al.

Title Page

Abstract

Introduction

Conclusions

References

Tables

Figures

◀

▶

◀

▶

Back

Close

Full Screen / Esc

Printer-friendly Version

Interactive Discussion

Model parameterizations were chosen to the best of our knowledge. It should, however, be noted that key processes such as glacial changes in POC burial efficiency are only poorly constrained by available data. Moreover, we assumed that the global mean morphology of continental margins was retained over the glacial cycle and that the average global change in relative sea-level was equal to eustatic sea-level change. This approach neglects the glacial isostatic adjustment, i.e. the glacial subsidence of northern land masses loaded by large ice sheets, the uplift in flanking regions, and the numerous far field effects (Daly, 1934; Milne and Mitrovica, 2008). It also neglects changes in margin morphology induced by the erosion and down-slope transport of shelf sediments during glacial sea-level low-stands (Hay, 1994) and the deglacial tilting of continental margins (Clark et al., 1978). Moreover, we assumed that during the LGM eustatic sea-level was 120 m lower than today while growing evidence supports the view that LGM sea-level fall was in fact larger than this consensus value (Austermann et al., 2013). The changes in the size of depositional and exposed areas at continental margins applied in the model should thus be regarded as rough estimates. Clearly, more work needs to be done to improve these estimates. However, there is no doubt that ocean margins retreated into steeper terrain while large shelf areas were exposed during glacial marine regressions and that these changes had a profound effect on glacial seawater composition and atmospheric $p\text{CO}_2$.

Appendix C: Model results

Key model results are listed in Tables C1 to C3 and compared to proxy data.

Appendix D: Radiocarbon model

A simple two-box-model helps to explain why the ocean is strongly depleted in radiocarbon with respect to the atmosphere when radiocarbon production rates are high. In

Effects of eustatic sea-level change, ocean dynamics, and iron fertilization on atmospheric $p\text{CO}_2$

K. Wallmann et al.

Title Page

Abstract

Introduction

Conclusions

References

Tables

Figures

◀

▶

◀

▶

Back

Close

Full Screen / Esc

Printer-friendly Version

Interactive Discussion

from the atmosphere are balanced (Eq. D2). The steady-state gradient ($^{14}\text{C}_A - ^{14}\text{C}_O$), thus, increases in proportion to the atmospheric production rate such that the flux into the ocean compensates for the elevated decay rate in the ocean. The analytical solution for the simple two-box-model (Eq. D4) correctly predicts the steady-state behavior of our more evolved model system where the ocean is represented by 24 boxes and the radiocarbon uptake from the atmosphere is calculated applying Eq. (A12) rather than Eq. (D3). It predicts that $\Delta\Delta^{14}\text{C-DIC}$ increases linearly with production rate as observed in the steady state simulations (Table C2). The real ocean–atmosphere system is obviously more complex than any kind of model. However, the simple 2-box-model captures the basic features of the real system and reveals that the ^{14}C contrast increases in proportion to the production rate. Since radiocarbon production rates may have changed significantly over the last glacial cycle, this basic system property has to be considered in the interpretation of the marine ^{14}C -record.

Acknowledgements. This work was funded by the DFG via the collaborative project SFB 754 and project Sa207/48-1. It gained from fruitful discussions with P. M. Grootes, Kiel.

The article processing charges for this open-access publication were covered by a Research Centre of the Helmholtz Association.

References

- Abe-Ouchi, A., Saito, F., Kawamura, K., Raymo, M. E., Okuno, J., Takahashi, K., and Blatter, H.: Insolation-driven 100,000-year glacial cycles and hysteresis of ice-sheet volume, *Nature*, 500, 190–193, doi:10.1038/nature12374, 2013.
- Adkins, J. F. and Boyle, E. A.: Changing atmospheric $\Delta^{14}\text{C}$ and the record of deep water paleoventilation ages, *Paleoceanography*, 12, 337–344, 1997.
- Altabet, M. A., Francois, R., Murray, D. W., and Prell, W. L.: Climate-related variations in denitrification in the Arabian Sea from sediment $^{15}\text{N}/^{14}\text{N}$ ratios, *Nature*, 373, 506–509, 1995.

Effects of eustatic sea-level change, ocean dynamics, and iron fertilization on atmospheric $p\text{CO}_2$

K. Wallmann et al.

[Title Page](#)[Abstract](#)[Introduction](#)[Conclusions](#)[References](#)[Tables](#)[Figures](#)[◀](#)[▶](#)[◀](#)[▶](#)[Back](#)[Close](#)[Full Screen / Esc](#)[Printer-friendly Version](#)[Interactive Discussion](#)

Anderson, R. F., Ali, S., Bradtmiller, L. I., Nielsen, S. H. H., Fleisher, M. Q., Anderson, B. E., and Burckle, L. H.: Wind-driven upwelling in the Southern Ocean and the deglacial rise in atmospheric CO_2 , *Science*, 323, 1443–1448, 2009.

Archer, D. E., Morford, J. L., and Emerson, S. R.: A model of suboxic sedimentary diagenesis suitable for automatic tuning and gridded global domains, *Global Biogeochem. Cy.*, 16, 1017, doi:10.1029/2000GB001288, 2002.

Aumont, O. and Bopp, L.: Globalizing results from ocean in situ iron fertilization studies, *Global Biogeochem. Cy.*, 20, GB2017, doi:10.1029/2005GB002591, 2006.

Austermann, J., Mitrovica, J. X., Latychev, K., and Milne, G. A.: Barbados-based estimate of ice volume at Last Glacial Maximum affected by subducted plate, *Nat. Geosci.*, 6, 553–557, 2013.

Barker, S., Knorr, G., Vautravers, M. J., Diz, P., and Skinner, L. C.: Extreme deepening of the Atlantic overturning circulation during deglaciation, *Nat. Geosci.*, 3, 567–571, 2010.

Baturin, G. N.: Issue of the relationship between primary productivity of organic carbon in ocean and phosphate accumulation (Holocene–Late Jurassic), *Lithol. Miner. Resour.*, 42, 318–348, 2007.

Baturin, G. N. and Savenko, V. S.: Phosphorus in oceanic sedimentogenesis, *Oceanology+*, 37, 107–113, 1997. (FOUND!)

Berelson, W. E., Balch, W. M., Najjar, R., Feely, R. A., Sabine, C., and Lee, K.: Relating estimates of CaCO_3 production, export, and dissolution in the water column to measurements of CaCO_3 rain into sediment traps and dissolution on the sea floor: A revised global carbonate budget, *Global Biogeochem. Cy.*, 21, GB1024, doi:10.1029/2006GB002803, 2007.

Berger, A. and Loutre, M. F.: Insolation values for the climate of the last 10 Million years, *Quaternary Sci. Rev.*, 10, 297–317, 1991.

Berger, W. H.: Increase of carbon dioxide in the atmosphere during deglaciation: the coral reef hypothesis, *Naturwissenschaften*, 69, 87–88, 1982.

Berner, R. A.: Burial of organic carbon and pyrite sulfur in the modern ocean: Its geochemical and environmental significance, *Am. J. Sci.*, 282, 451–473, 1982.

Berner, R. A.: *The Phanerozoic Carbon Cycle: CO_2 and O_2* , Oxford University Press, Oxford, 150 pp., 2004.

Berner, R. A. and Rao, J.-J.: Phosphorus in sediments of the Amazon River and estuary: implications for the global flux of phosphorus to the sea, *Geochim. Cosmochim. Ac.*, 58, 2333–2339, 1994.

Effects of eustatic sea-level change, ocean dynamics, and iron fertilization on atmospheric $p\text{CO}_2$

K. Wallmann et al.

[Title Page](#)[Abstract](#)[Introduction](#)[Conclusions](#)[References](#)[Tables](#)[Figures](#)[◀](#)[▶](#)[◀](#)[▶](#)[Back](#)[Close](#)[Full Screen / Esc](#)[Printer-friendly Version](#)[Interactive Discussion](#)

- Bohlen, L., Dale, A., and Wallmann, K.: Simple transfer functions for calculating benthic fixed nitrogen losses and C:N:P regeneration ratios in global biogeochemical models, *Global Biochem. Cy.*, 26, GB3029, doi:10.1029/2011GB004198, 2012.
- Bordelon-Katrynski, L. A. and Schneider, B.: Feedbacks of CO_2 dependent dissolved organic carbon production on atmospheric CO_2 in an ocean biogeochemical model, *Biogeosciences Discuss.*, 9, 7983–8011, doi:10.5194/bgd-9-7983-2012, 2012.
- Boyle, E. A. and Keigwin, L. D.: Deep circulation of the North Atlantic over the last 200,000 years: geochemical evidence, *Science*, 218, 784–787, 1982.
- Broecker, W. S.: Ocean chemistry during glacial time, *Geochim. Cosmochim. Ac.*, 46, 1689–1705, 1982.
- Broecker, W. S.: The great ocean conveyor, *Oceanography*, 4, 79–90, 1991.
- Broecker, W. S., Peacock, S. L., Walker, S., Weiss, R., Fahrback, E., Schroeder, M., Mikolajewicz, U., Heinze, C., Key, R., Peng, T.-H., and Rubin, S.: How much deep water is formed in the Southern Ocean?, *J. Geophys. Res.*, 103, 15833–15843, 1998.
- Broecker, W. S., Clark, E., Hajdas, I., and Bonani, G.: Glacial ventilation rates for the deep Pacific Ocean, *Paleoceanography*, 19, PA2002, doi:10.1029/2003PA000974, 2004.
- Brovkin, V. and Ganopolski, A.: The role of the terrestrial biosphere in CLIMBER-2 simulations of the last 4 glacial CO_2 cycles, *Nova Act. Lc.*, 121, 43–47, 2015.
- Brovkin, V., Ganopolski, A., Archer, D., and Munhoven, G.: Glacial CO_2 cycle as a succession of key physical and biogeochemical processes, *Clim. Past*, 8, 251–264, doi:10.5194/cp-8-251-2012, 2012.
- Bryan, S. P., Marchitto, T. M., and Lehman, S. J.: The release of ^{14}C -depleted carbon from the deep ocean during the last deglaciation: evidence from the Arabian Sea, *Earth Planet. Sci. Lett.*, 298, 244–254, 2010.
- Burdige, D. J.: Preservation of organic matter in marine sediments: controls, mechanisms, and an imbalance in sediment organic carbon budgets?, *Chem. Rev.*, 107, 467–485, 2007.
- Burke, W. H., Denison, R. E., Hetherington, E. A., Koepnick, R. B., Nelson, H. F., and Otto, J. B.: Variation of seawater $^{87}\text{Sr}/^{86}\text{Sr}$ throughout Phanerozoic time, *Geology*, 10, 516–519, 1982.
- Burwicz, E. B., Rüpke, L. H., and Wallmann, K.: Estimation of the global amount of submarine gas hydrates formed via microbial methane formation based on numerical reaction-transport modeling and a novel parameterization of Holocene sedimentation, *Geochim. Cosmochim. Ac.*, 75, 4562–4576, 2011.

Effects of eustatic sea-level change, ocean dynamics, and iron fertilization on atmospheric $p\text{CO}_2$

K. Wallmann et al.

[Title Page](#)
[Abstract](#)
[Introduction](#)
[Conclusions](#)
[References](#)
[Tables](#)
[Figures](#)




[Back](#)
[Close](#)
[Full Screen / Esc](#)
[Printer-friendly Version](#)
[Interactive Discussion](#)

- Clark, J. A., Farrell, W. E., and Peltier, W. R.: Global changes in postglacial sea level: a numerical calculation, *Quaternary Sci. Rev.*, 9, 265–287, 1978.
- Conkright, M. E., Locarnini, R. A., Garcia, H. E., O'Brien, T. D., Boyer, T. P., Stephens, C., and J. I. Antonov: World Ocean Atlas 2001: Objective Analyses, Data Statistics, and Figures, National Oceanographic Data Center, Silver Spring, MD, 17, 2002.
- Curry, W. B. and Oppo, D. W.: Glacial water mass geometry and the distribution of $\delta^{13}\text{C}$ of ΣCO_2 in the western Atlantic Ocean, *Paleoceanography*, 20, PA1017, doi:10.1029/2004PA001021, 2005.
- Dale, A. W., Sommer, S., Lomnitz, U., Montes, I., Treude, T., Liebetrau, V., Gier, J., Hensen, C., Dengler, M., Stolpovsky, K., Bryant, L. D., and Wallmann, K.: Organic carbon production, mineralisation and preservation on the Peruvian margin, *Biogeosciences*, 12, 1537–1559, doi:10.5194/bg-12-1537-2015, 2015.
- Daly, R. A.: *The Changing World of the Ice Age*, Yale University Press, New Haven, 1934.
- Denton, G. H., Anderson, R. F., Toggweiler, J. R., Edwards, R. L., Schaefer, J. M., and Putnam, A. E.: The Last Glacial Termination, *Science*, 328, 1652–1656, 2010.
- Deutsch, C., Gruber, N., Key, R. M., and Sarmiento, J. L.: Denitrification and N_2 fixation in the Pacific Ocean, *Global Biogeochem. Cy.*, 15, 483–506, 2001.
- Deutsch, C., Sigman, D. M., Thunell, R. C., Meckler, A. N., and Haug, G. H.: Isotopic constraints on glacial/interglacial changes in the oceanic nitrogen budget, *Global Biogeochem. Cy.*, 18, GB4012, doi:10.1029/2003GB002189, 2004.
- Dunne, J. P., Sarmiento, J. L., and Gnanadesikan, A.: A synthesis of global particle export from the surface ocean and cycling through the ocean interior and on the seafloor, *Global Biogeochem. Cy.*, 21, GB4006, doi:10.1029/2006GB002907, 2007.
- Duplessy, J. C., Shackleton, N. J., Fairbanks, R. G., Labeyrie, L., Oppo, D., and Kallel, N.: Deepwater source variations during the last climatic cycle and their impact on the global deepwater circulation, *Paleoceanography*, 3, 343–360, 1988.
- Eakins, B. W. and Sharman, G. F.: *Hypsographic curve of Earth's surface from ETOPO1*, NOAA National Geophysical Data Center, Boulder, CO, 2012.
- Eugster, O., Gruber, N., Deutsch, C., Jaccard, S. L., and Payne, M. R.: The dynamics of the marine nitrogen cycle across the last deglaciation, *Paleoceanography*, 28, 116–129, doi:10.1002/palo.20020, 2013.

Effects of eustatic sea-level change, ocean dynamics, and iron fertilization on atmospheric $p\text{CO}_2$

K. Wallmann et al.

[Title Page](#)[Abstract](#)[Introduction](#)[Conclusions](#)[References](#)[Tables](#)[Figures](#)[◀](#)[▶](#)[◀](#)[▶](#)[Back](#)[Close](#)[Full Screen / Esc](#)[Printer-friendly Version](#)[Interactive Discussion](#)

Frank, M., Schwarz, B., Baumann, S., Kubik, P. W., Suter, M., and Mangini, A.: A 200 kyr record of cosmogenic radionuclide production rate and geomagnetic field intensity from ^{10}Be in globally stacked deep-sea sediments, *Earth Planet. Sc. Lett.*, 149, 121–129, 1997.

Franke, J., Paul, A., and Schulz, M.: Modeling variations of marine reservoir ages during the last 45 000 years, *Clim. Past*, 4, 125–136, doi:10.5194/cp-4-125-2008, 2008.

Froelich, P. N., Bender, M. L., Luedtke, N. A., Heath, G. R., and DeVries, T.: The marine phosphorus cycle, *Am. J. Sci.*, 282, 474–511, 1982.

Ganopolski, A. and Calov, R.: The role of orbital forcing, carbon dioxide and regolith in 100 kyr glacial cycles, *Clim. Past*, 7, 1415–1425, doi:10.5194/cp-7-1415-2011, 2011.

Ganopolski, A., Rahmstorf, S., Petoukhov, V., and Claussen, M.: Simulation of modern and glacial climates with a coupled global model of intermediate complexity, *Nature*, 391, 351–356, 1998.

Ganopolski, A., Calov, R., and Claussen, M.: Simulation of the last glacial cycle with a coupled climate ice-sheet model of intermediate complexity, *Clim. Past*, 6, 229–244, doi:10.5194/cp-6-229-2010, 2010.

García, H. E. and Gordon, L. I.: Oxygen solubility in seawater: better fitting equations, *Limnol. Oceanogr.*, 37, 1307–1312, 1992.

Gebhardt, H., Sarnhein, M., Grootes, P. M., Kiefer, T., Kuehn, H., Schmieder, F., and Röhl, U.: Paleonutrient and productivity records from the subarctic North Pacific for Pleistocene glacial terminations I to V, *Paleoceanography*, 23, PA4212, doi:10.1029/2007PA001513, 2008.

Gnanadesekian, A. and Hallberg, R.: Physical oceanography, thermal structure and general circulation, in: *Encyclopedia of Physical Science and Technology*, edited by: Meyers, R. A., Academic Press, San Diego, 189–210, 2002.

Hartnett, H. E., Keil, R. G., Hedges, J. I., and Devol, A. H.: Influence of oxygen exposure time on organic carbon preservation in continental margin sediments, *Nature*, 391, 572–574, 1998.

Hay, W. W.: Pleistocene-Holocene fluxes are not the Earth's norm, in: *Material Fluxes on the Surface of the Earth*, edited by: Hay, W. W. and Usselman, T., Studies in Geophysics, National Academy Press, Washington, 15–27, 1994.

Hay, W. W. and Southam, J. R.: Modulation of marine sedimentation by the continental shelves, in: *The Fate of Fossil Fuel CO_2 in the Oceans*, edited by: Andersen, N. R. and Malahoff, A., Plenum Press, New York, 569–604, 1977.

Honjo, S., Manganini, S. J., Krishfield, R. A., and Francois, R.: Particulate organic carbon fluxes to the ocean interior and factors controlling the biological pump: A syn-

Effects of eustatic sea-level change, ocean dynamics, and iron fertilization on atmospheric $p\text{CO}_2$

K. Wallmann et al.

[Title Page](#)[Abstract](#)[Introduction](#)[Conclusions](#)[References](#)[Tables](#)[Figures](#)[⏪](#)[⏩](#)[◀](#)[▶](#)[Back](#)[Close](#)[Full Screen / Esc](#)[Printer-friendly Version](#)[Interactive Discussion](#)

thesis of global sediment trap programs since 1983, *Prog. Oceanogr.*, 76, 217–285, doi:10.1016/j.pocean.2007.11.003, 2008.

Imbrie, J. and Imbrie, J. Z.: Modeling the climatic response to orbital variations, *Science*, 207, 943–953, 1980.

5 Imbrie, J., Berger, A., E. A., B., Clemens, S. C., Duffy, A., Howard, W. R., Kukja, G., Kutzbach, J., Martinson, D. G., McIntyre, A., Mix, A. C., Molfino, B., Morley, J. J., Peterson, L. C., Pjsias, N. G., Prell, W. L., Raymo, M. E., Shackleton, N. J., and Toggweiler, J. R.: On the structure and origin of major glaciation cycles. 2. The 100,000-year cycle, *Paleoceanography*, 8, 699–735, 1993.

10 Jaccard, S. L. and Galbraith, E. D.: Large climate-driven changes of oceanic oxygen concentrations during the last deglaciation, *Nat. Geosci.*, 5, 151–156, 2012.

Jahnke, R. A.: The global ocean flux of particulate organic carbon: Areal distribution and magnitude, *Global Biogeochem. Cy.*, 10, 71–88, 1996.

15 Key, R. M., Kozyr, A., Sabine, C. L., Lee, K., Wanninkhof, R., Bullister, J. L., Feely, R. A., Millero, F. J., Mordy, C., and Peng, T.-H.: A global ocean carbon climatology: results from Global Data Analysis Project (GLODAP), *Global Biogeochem. Cy.*, 18, GB4031, doi:10.1029/2004GB002247, 2004.

Kleypas, J. A.: Modeled estimates of global reef habitat and carbonate production since the last glacial maximum, *Paleoceanography*, 12, 533–545, 1997.

20 Köhler, P. and Fischer, H.: Simulating changes in the terrestrial biosphere during the last glacial/interglacial transition, *Global Planet. Change*, 43, 33–55, 2004.

Köhler, P., Fischer, H., Munhoven, G., and Zeebe, R. E.: Quantitative interpretation of atmospheric carbon records over the last glacial termination, *Global Biochem. Cy.*, 19, GB4020, doi:10.1029/2004GB002345, 2005.

25 Köhler, P., Muscheler, R., and Schmitt, J.: A model-based interpretation of low-frequency changes in the carbon cycle during the last 120,000 years and its implications for the reconstruction of atmospheric $\Delta^{14}\text{C}$, *Geochem. Geophys. Geosy.*, 7, Q11N06, doi:10.1029/2008PA001703, 2006.

Körtzinger, A., Hedges, J. I., and Quay, P. D.: Redfield ratios revisited: Removing the biasing effect of anthropogenic CO_2 , *Limnol. Oceanogr.*, 46, 964–970, 2001.

30 Laj, C., Kissel, C., Mazaud, A., Michel, E., Muscheler, R., and Beer, J.: Geomagnetic field intensity, North Atlantic Deep Water circulation and atmospheric $\Delta^{14}\text{C}$ during the last 50 kyr, *Earth Planet. Sc. Lett.*, 200, 177–190, 2002.

Effects of eustatic sea-level change, ocean dynamics, and iron fertilization on atmospheric $p\text{CO}_2$

K. Wallmann et al.

Title Page

Abstract

Introduction

Conclusions

References

Tables

Figures

◀

▶

◀

▶

Back

Close

Full Screen / Esc

Printer-friendly Version

Interactive Discussion

- Madec, G., Delecluse, P., Imbard, M., and Levy, C.: OPA8.1 Ocean general circulation model reference manual, Notes du pôle de modél. 11, Inst. Pierre-Simon Laplace, Paris, 91, 1998.
- Marcott, S. A., Bauska, T. K., Buizert, C., Steig, E. J., Rosen, J. L., Cuffey, K. M., Fudge, T. J., Severinghaus, J. P., Ahn, J., Kalk, M. L., McConnell, J. R., Sowers, T., Taylor, K. C., White, J. W. C., and Brook, E. J.: Centennial-scale changes in the global carbon cycle during the last deglaciation, *Nature*, 514, 616–619, 2014.
- Marinov, I., Gnanadesikan, A., Toggweiler, J. R., and Sarmiento, J. L.: The Southern Ocean biogeochemical divide, *Nature*, 441, 964–967, 2006.
- Martin, J. H.: Glacial-interglacial CO_2 change: the iron hypothesis, *Paleoceanography*, 5, 1–13, 1990.
- Martinez-Garcia, A., Sigman, D. M., Ren, H., Anderson, R. F., Straub, M., Hodell, D. A., Jacobson, S. L., Eglinton, T. I., and Haug, G. H.: Iron fertilization of the Subantarctic Ocean during the last ice age, *Science*, 343, 1347–1350, 2014.
- Mayer, L. M., Schick, L. L., Hardy, K. R., Wagal, R., and McCarthy, J.: Organic matter in small mesopores in sediments and soils, *Geochim. Cosmochim. Ac.*, 68, 3863–3872, 2004.
- McManus, J. F., Francois, R., Gherardi, J.-M., Keigwin, L. D., and Brown-Leger, S.: Collapse and rapid resumption of Atlantic meridional circulation linked to deglacial climate changes, *Nature*, 428, 834–837, 2004.
- Middelburg, J. J., Soetaert, K., Herman, P. M. J., and Heip, C. H. R.: Denitrification in marine sediments: A model study, *Global Biogeochem. Cy.*, 10, 661–673, 1996.
- Milankovitch, M.: Kanon der Erdbestrahlung und Seine Anwendung auf das Eiszeitenproblem, Royal Serbian Academy Special Publication, Royal Serbian Academy, Belgrade, Serbia, 1941.
- Milliman, J. D. and Droxler, A. W.: Neritic and pelagic carbonate sedimentation in the marine environment: ignorance is not a bliss, *Geol. Rundsch.*, 85, 496–504, 1996.
- Milne, G. A. and Mitrovica, J. X.: Searching for eustasy in deglacial sea-level histories, *Quaternary Sci. Rev.*, 27, 2292–2302, 2008.
- Monnin, E., Indermühle, A., Dallenbach, A., Flückiger, J., Stauffer, B., Stocker, T. F., Raynaud, D., and Barnola, J.-M.: Atmospheric CO_2 concentrations over the Last Glacial Termination, *Science*, 291, 112–114, 2001.
- Monnin, E., Steig, E. J., Siegenthaler, U., Kawamura, K., Schwander, J., Stauffer, B., Stocker, T. F., Morse, D. L., Barnola, J.-M., Bellier, B., Raynaud, D., and Fischer, H.: Evidence for substantial accumulation rate variability in Antarctica during the Holocene, through

Effects of eustatic sea-level change, ocean dynamics, and iron fertilization on atmospheric $p\text{CO}_2$

K. Wallmann et al.

[Title Page](#)[Abstract](#)[Introduction](#)[Conclusions](#)[References](#)[Tables](#)[Figures](#)[◀](#)[▶](#)[◀](#)[▶](#)[Back](#)[Close](#)[Full Screen / Esc](#)[Printer-friendly Version](#)[Interactive Discussion](#)

synchronization of CO_2 in the Taylor Dome, Dome C and DML ice cores, *Earth Planet. Sc. Lett.*, 224, 45–54, 2004.

Mook, W. G. and van der Plicht, J.: Reporting C-14 activities and concentrations, *Radiocarbon*, 41, 227–239, 1999.

5 Munhoven, G.: Glacial-interglacial changes of continental weathering: estimates of the related CO_2 and HCO_3^- flux variations and their uncertainties, *Global Planet. Change*, 33, 155–176, 2002.

Muscheler, R., Beer, J., Kubik, P. W., and Synal, H.-A.: Geomagnetic field intensity during the last 60,000 years based on ^{10}Be and ^{36}Cl from the Summit ice cores and ^{14}C , *Quaternary Sci. Rev.*, 24, 1849–1860, 2005.

10 Oliver, K. I. C., Hoogakker, B. A. A., Crowhurst, S., Henderson, G. M., Rickaby, R. E. M., Edwards, N. R., and Elderfield, H.: A synthesis of marine sediment core $\delta^{13}\text{C}$ data over the last 150 000 years, *Clim. Past*, 6, 645–673, doi:10.5194/cp-6-645-2010, 2010.

Opdyke, B. N. and Walker, J. C. G.: Return of the coral reef hypothesis: Basin to shelf partitioning of CaCO_3 and its effect on atmospheric CO_2 , *Geology*, 20, 733–736, 1992.

15 Peterson, C. D., Lisiecki, L. E., and Stern, J. V.: Deglacial whole-ocean $\delta^{13}\text{C}$ change estimated from 480 benthic foraminiferal records, *Paleoceanography*, 29, 549–563, doi:10.1002/2013PA002552, 2014.

20 Petit, L. R., Jouzel, J., Raynaud, D., Barkov, N. I., Barnola, J.-M., Basile, I., Bender, M., Chappelaz, J., Davis, M., Delaygue, G., Delmotte, M., Kotlyakov, V. M., Legrand, M., Lipenkov, V. Y., Lorius, C., Pépin, L., Ritz, C., Saltzman, E., and Stievenard, M.: Climate and atmospheric history of the past 420,000 years from the Vostok ice core, Antarctica, *Nature*, 399, 429–436, 1999.

25 Piotrowski, A. M., Goldstein, S. L., Hemming, S. R., and Fairbanks, R. G.: Temporal relationships of carbon cycling and ocean circulation at glacial boundaries, *Science*, 307, 1933–1937, 2005.

Pollard, D.: Ice-age simulations with a calving ice-sheet model, *Quaternary Res.*, 20, 30–48, 1983.

30 Rae, J. W. B., Sarinthein, M., Foster, G. L., Ridgwell, A., Grootes, P. M., and Elliott, T.: Deep water formation in the North Pacific and deglacial CO_2 rise, *Paleoceanography*, 29, 645–667, doi:10.1002/2013PA002570, 2014.

Effects of eustatic sea-level change, ocean dynamics, and iron fertilization on atmospheric $p\text{CO}_2$

K. Wallmann et al.

[Title Page](#)
[Abstract](#)
[Introduction](#)
[Conclusions](#)
[References](#)
[Tables](#)
[Figures](#)




[Back](#)
[Close](#)
[Full Screen / Esc](#)
[Printer-friendly Version](#)
[Interactive Discussion](#)

- Raitzsch, M., Hathorne, E. C., Kuhnert, H., Groeneveld, J., and Bickert, T.: Modern and late Pleistocene B/Ca ratios of the benthic foraminifer *Planulina wuellerstorfi* determined with laser ablation ICP-MS, *Geology*, 39, 1039–1042, 2011.
- Raymo, M. E., Oppo, D. W., and Curry, W.: The mid-Pleistocene climate transition: a deep sea carbon isotope perspective, *Paleoceanography*, 12, 546–559, 1997.
- Redfield, A. C.: The biological control of chemical factors in the environment, *Am. Sci.*, 46, 205–221, 1958.
- Reimer, P. J., Bard, E., Bayliss, A., Beck, J. W., Blackwell, P. G., Ramsey, C. B., Buck, C. E., Cheng, H., Edwards, R. L., Friedrich, M., Grootes, P. M., Guilderson, T. P., Hafliadason, H., Hajdas, I., Hatté, C., Heaton, T. J., Hoffmann, D. L., Hogg, A. G., Hughen, K. A., Kaiser, K. F., Kromer, B., Manning, S. W., Niu, M., Reimer, R. W., Richards, D. A., Scott, E. M., Southon, J. R., Staff, R. A., Turney, C. S. M., and van der Plicht, J.: IntCal13 and marine13 radiocarbon age calibration curves 0–50,000 years Cal BP, *Radiocarbon*, 55, 1869–1887, 2013.
- Ridgwell, A.: Glacial-interglacial perturbations in the global carbon cycle, PhD, University of East Anglia, Norwich, UK, 2001.
- Roberts, N. L., Piotrowski, A. M., McManus, J. F., and Keigwin, L. D.: Synchronous deglacial overturning and water mass source changes, *Science*, 327, 75–78, 2010.
- Robinson, L. F., Adkins, J. F., Keigwin, L. D., Southon, J., Fernandez, D. P., Wang, S.-L., and Scheirer, D. S.: Radiocarbon variability in the Western North Atlantic during the last deglaciation, *Science*, 310, 1469–1473, 2005.
- Romanek, C. S., Grossman, E. L., and Morse, J. W.: Carbon isotope fractionation in synthetic aragonite and calcite: effects of temperature and precipitation rate, *Geochim. Cosmochim. Ac.*, 56, 419–430, 1992.
- Ruttenberg, K. C.: Development of a sequential extraction method for different forms of phosphorus in marine sediments, *Limnol. Oceanogr.*, 37, 1460–1482, 1992.
- Ruttenberg, K. C. and Berner, R. A.: Authigenic apatite formation and burial in sediments from non-upwelling, continental margin environments, *Geochim. Cosmochim. Ac.*, 57, 991–1007, 1993.
- Sarmiento, J. L. and Gruber, N.: *Ocean Biogeochemical Cycles*, Princeton University Press, Princeton, 503 pp., 2006.

Effects of eustatic sea-level change, ocean dynamics, and iron fertilization on atmospheric $p\text{CO}_2$

K. Wallmann et al.

[Title Page](#)
[Abstract](#)
[Introduction](#)
[Conclusions](#)
[References](#)
[Tables](#)
[Figures](#)




[Back](#)
[Close](#)
[Full Screen / Esc](#)
[Printer-friendly Version](#)
[Interactive Discussion](#)

Sarnthein, M., Winn, K., Jung, S. J. A., Duplessy, J.-C., Labeyrie, L., Erlenkeuser, H., and Ganssen, G.: Changes in east Atlantic deepwater circulation over the last 30,000 years: eight time slice reconstructions, *Paleoceanography*, 9, 209–267, 1994.

Sarnthein, M., Schneider, B., and Grootes, P. M.: Peak glacial ^{14}C ventilation ages suggest major draw-down of carbon into the abyssal ocean, *Clim. Past*, 9, 2595–2614, doi:10.5194/cp-9-2595-2013, 2013.

Sarnthein, M., Balmer, S., Grootes, P. M., and Mudelsee, M.: Planktic and benthic ^{14}C reservoir ages for three ocean basins, calibrated by a suite of ^{14}C plateaus in the glacial-to-deglacial Suigetsu atmospheric ^{14}C record, *Radiocarbon*, 57, 129–151, doi:10.2458/azu_rc.57.17916, 2015.

Schlünz, B., Schneider, R. R., Müller, P. J., Swowers, W. J., and Wefer, G.: Terrestrial organic carbon accumulation on the Amazon deep sea fan during the glacial sea level stand, *Chem. Geol.*, 159, 263–281, 1999.

Schmitt, J., Schneider, R., Elsig, J., Leuenberger, D., Laurantou, A., Chappellaz, J., Köhler, P., Joos, F., Stocker, T. F., Leuenberger, M., and Fischer, H.: Carbon isotope constraints on the deglacial CO_2 rise from ice cores, *Science*, 336, 711–714, 2012.

Schmittner, A., Urban, N. M., Shakun, J. D., Mahowald, N. M., Clark, P. U., Bartlein, P. J., Mix, A. C., and Rosell-Melé, A.: Climate sensitivity estimated from temperature reconstructions of the Last Glacial Maximum, *Science*, 334, 1385–1388, 2011.

Schmittner, A., Gruber, N., Mix, A. C., Key, R. M., Tagliabue, A., and Westberry, T. K.: Biology and air–sea gas exchange controls on the distribution of carbon isotope ratios ($\delta^{13}\text{C}$) in the ocean, *Biogeosciences*, 10, 5793–5816, doi:10.5194/bg-10-5793-2013, 2013.

Seiter, K., Hensen, C., and Zabel, M.: Benthic carbon mineralization on a global scale, *Global Biogeochem. Cy.*, 19, GB1010, doi:10.1029/2004GB002225, 2005.

Shackleton, N. J.: Carbon-13 in *Uvigerina*: Tropical rainforest history in the equatorial Pacific carbonate dissolution cycles, in: *The Fate of Fossil Fuel in the Oceans*, edited by: Andersen, N. R., and Malahoff, A., Plenum, New York, 401–427, 1977.

Skinner, L. C.: Glacial-interglacial atmospheric CO_2 change: a possible “standing volume” effect on deep-ocean carbon sequestration, *Clim. Past*, 5, 537–550, doi:10.5194/cp-5-537-2009, 2009.

Skinner, L. C., Fallon, S., Waelbroeck, C., Michel, E., and Barker, S.: Ventilation of the deep Southern Ocean and deglacial CO_2 rise, *Science*, 328, 1147–1151, 2010.

Effects of eustatic sea-level change, ocean dynamics, and iron fertilization on atmospheric $p\text{CO}_2$

K. Wallmann et al.

[Title Page](#)
[Abstract](#)
[Introduction](#)
[Conclusions](#)
[References](#)
[Tables](#)
[Figures](#)




[Back](#)
[Close](#)
[Full Screen / Esc](#)
[Printer-friendly Version](#)
[Interactive Discussion](#)

- Skinner, L. C., Waelbroeck, C., Scrivner, A. E., and Fallon, S. J.: Radiocarbon evidence for alternating northern and southern sources of ventilation of the deep Atlantic carbon pool during the last deglaciation, *P. Natl. Acad. Sci. USA*, 111, 5480–5484, 2014.
- Stanford, J. D., Hemingway, R., Rohling, E. J., Challenor, P. G., Medina-Elizalde, M., and Lester, A. J.: Sea-level probability for the last deglaciation: a statistical analysis of far-field records, *Global Planet. Change*, 79, 193–203, 2011.
- Stuiver, M. and Polach, H. A.: Discussion: reporting of ^{14}C data, *Radiocarbon*, 19, 355–363, 1977.
- Suess, E.: Particulate organic carbon flux in the oceans – surface productivity and oxygen utilization, *Nature*, 288, 260–263, 1980.
- Tamburini, F. and Föllmi, K. B.: Phosphorus burial in the ocean over glacial-interglacial time scales, *Biogeosciences*, 6, 501–513, doi:10.5194/bg-6-501-2009, 2009.
- Thornalley, D. J. R., Barker, S., Broecker, W. S., Elderfield, H., and McCave, N.: The deglacial evolution of North Atlantic deep convection, *Science*, 331, 202–205, 2011.
- Toggweiler, J. R.: Variation of atmospheric CO_2 by ventilation of the ocean's deepest water, *Paleoceanography*, 14, 571–588, 1999.
- Tyrrell, T.: The relative influences of nitrogen and phosphorus on oceanic primary production, *Nature*, 400, 525–531, 1999.
- Ushie, H. and Matsumoto, K.: The role of shelf nutrients on glacial-interglacial CO_2 : A negative feedback, *Global Biogeochem. Cy.*, 26, GB2039, doi:10.1029/2011GB004147, 2012.
- Waelbroeck, C., Labeyrie, L., Michel, E., Duplessy, J.-C., McManus, J. F., Lambeck, K., Balbon, E., and Labracherie, M.: Sea-level and deep water temperature changes derived from benthic foraminifera isotopic records, *Quaternary Sci. Rev.*, 21, 295–305, 2002.
- Wallmann, K.: Phosphorus imbalance in the global ocean?, *Global Biogeochem. Cy.*, 24, GB4030, doi:10.1029/2009GB003643, 2010.
- Wallmann, K.: Is late Quaternary climate change governed by self-sustained oscillations in atmospheric CO_2 ?, *Geochim. Cosmochim. Ac.*, 132, 413–439, 2014.
- Wallmann, K., Pinero, E., Burwicz, E., Haeckel, M., Hensen, C., Dale, A., and Ruepke, L.: The global inventory of methane hydrate in marine sediments: a theoretical approach, *Energies*, 5, 2449–2498, 2012.
- Walsh, J. J., Rowe, G. T., Iverson, R. L., and McRoy, C. P.: Biological export of shelf carbon is a sink of the global CO_2 cycle, *Nature*, 291, 196–201, 1981.

Effects of eustatic sea-level change, ocean dynamics, and iron fertilization on atmospheric $p\text{CO}_2$

K. Wallmann et al.

[Title Page](#)[Abstract](#)[Introduction](#)[Conclusions](#)[References](#)[Tables](#)[Figures](#)[◀](#)[▶](#)[◀](#)[▶](#)[Back](#)[Close](#)[Full Screen / Esc](#)[Printer-friendly Version](#)[Interactive Discussion](#)

Yu, J., Elderfield, H., and Piotrowski, A. M.: Seawater carbonate ion- $\delta^{13}\text{C}$ systematics and application to glacial-interglacial North Atlantic ocean circulation, *Earth Planet. Sc. Lett.*, 271, 209–220, 2008.

Yu, J., Broecker, W. S., Elderfield, H., Jin, Z., McManus, J., and Zhang, F.: Loss of carbon from the deep sea since the Last Glacial Maximum, *Science*, 330, 1084–1087, 2010.

Yu, J., Anderson, R. F., Jin, Z., Rae, J. W. B., Opydyke, B. N., and Eggins, S. M.: Responses of the deep ocean carbonate system to carbon reorganization during the Last Glacial-interglacial cycle, *Quaternary Sci. Rev.*, 76, 39–52, 2013.

Yu, J., Anderson, R. F., Jin, Z., Menviel, L., Zhang, F., Ryerson, F. J., and Rohling, E. J.: Deep South Atlantic carbonate chemistry and increased interocean deep water exchange during last deglaciation, *Quaternary Sci. Rev.*, 90, 80–89, 2014.

Zeebe, R. and Wolf-Gladrow, D.: CO_2 in Seawater: Equilibrium, Kinetics and Isotopes, Elsevier Oceanography Series, Elsevier, Amsterdam, 346 pp., 2001.

Zhang, J., Quay, P. D., and Wilbur, D. O.: Carbon-isotope fractionation during gas-water exchange and dissolution of CO_2 , *Geochim. Cosmochim. Ac.*, 59, 107–114, 1995.

Table 1. Controls on atmospheric $p\text{CO}_2$ and mean dissolved carbon and phosphorus concentrations in the global ocean.

Simulation	$p\text{CO}_2$ at 21 ka in ppmv	$p\text{CO}_2$ at 0 ka in ppmv	DIC at 21 ka in μM	DIC at 0 ka in μM	DP at 21 ka in μM	DP at 0 ka in μM
STD (standard simulation)	190	279	2465	2300	2.44	2.14
STD with constant SST	206	275	2453	2289	2.48	2.15
STD with constant salinity	185	291	2466	2301	2.44	2.14
STD with constant salinity and constant ocean volume	177	281	2409	2310	2.41	2.16
STD with constant riverine DP flux	240	345	2564	2430	2.16	1.98
STD with constant rates of chemical weathering	193	268	2355	2202	2.15	1.98
STD with constant deposi- tional area for P burial	263	367	2599	2478	2.03	1.95
STD with constant deposi- tional area for POC burial	129	180	2132	1925	2.42	2.07
STD with constant burial rate of neritic carbonates	200	277	2437	2291	2.46	2.15
STD-CC-CN	234	255	2400	2273	2.68	2.30
STD with constant AMOC	200	262	2381	2233	2.49	2.12
STD-CC	203	263	2364	2240	2.31	2.14

Effects of eustatic sea-level change, ocean dynamics, and iron fertilization on atmospheric $p\text{CO}_2$

K. Wallmann et al.

Title Page

Abstract

Introduction

Conclusions

References

Tables

Figures

◀

▶

◀

▶

Back

Close

Full Screen / Esc

Printer-friendly Version

Interactive Discussion

Effects of eustatic sea-level change, ocean dynamics, and iron fertilization on atmospheric $p\text{CO}_2$

K. Wallmann et al.

[Title Page](#)
[Abstract](#)
[Introduction](#)
[Conclusions](#)
[References](#)
[Tables](#)
[Figures](#)
[Back](#)
[Close](#)
[Full Screen / Esc](#)
[Printer-friendly Version](#)
[Interactive Discussion](#)

Table A1. Salinity (Sal in PSU), dissolved phosphate, nitrate, and oxygen in model boxes (in μM): model vs. data. Subscripts: S: surface water (0–100 m), I: intermediate water (100–2000 m), D: deep water (2000–4000 m), B: bottom water (> 4000 m).

Box	Sal data	Sal model	PO ₄ data	PO ₄ model	NO ₃ data	NO ₃ model	O ₂ data	O ₂ model
NA _S	35.55	35.24	0.29	0.325	4.0	4.67	257.2	248
TA _S	36.22	36.1	0.31	0.335	3.09	4.19	201.6	212
SO _S	34.5	34.3	1.05	1.08	13.01	14.2	290.3	284
TIP _S	35.03	34.95	0.4	0.447	3.03	4.34	198.9	208
NP _S	33.6	33.59	0.84	0.781	8.15	9.88	276.0	263
AR _S	32.96	33.01	0.84	0.825	6.58	11.1	340.7	349
NA _I	35.28	35.05	0.87	1.12	16.29	16.8	238.6	234
TA _I	34.99	34.93	1.63	1.72	25.1	25.5	181.5	169
SO _I	34.58	34.54	1.98	2.05	28.43	29.1	209.7	212
TIP _I	34.68	34.64	2.37	2.43	32.16	34.1	107.1	93.4
NP _I	34.32	34.52	2.75	2.67	38.17	35.7	73.65	90.7
AR _I	34.83	34.82	0.99	0.961	13.22	13.4	296.7	313
NA _D	34.95	34.92	1.18	1.19	18.71	16.9	265.1	257
TA _D	34.92	34.9	1.43	1.54	21.67	21.8	245.5	220
SO _D	34.72	34.76	2.2	2.14	31.32	29.2	203.7	211
TIP _D	34.69	34.75	2.49	2.53	35.5	33.9	145.5	149
NP _D	34.65	34.69	2.73	2.57	38.63	34.1	116.0	134
AR _D	34.94	34.87	1.04	1.07	14.69	15	287.0	287
NA _B	34.9	34.91	1.33	1.42	20.18	19.3	260.5	237
TA _B	34.86	34.87	1.56	1.64	23.81	23	242.4	217
SO _B	34.7	34.76	2.22	2.16	32.07	29.4	220.2	206
TIP _B	34.7	34.75	2.34	2.39	33.65	31.8	176.4	173
NP _B	34.69	34.71	2.51	2.52	36.02	33.4	155.9	144
AR _B	34.94	34.87	1.05	1.08	14.6	15.2	276.5	285

Effects of eustatic sea-level change, ocean dynamics, and iron fertilization on atmospheric $p\text{CO}_2$

K. Wallmann et al.

[Title Page](#)
[Abstract](#)
[Introduction](#)
[Conclusions](#)
[References](#)
[Tables](#)
[Figures](#)
[Back](#)
[Close](#)
[Full Screen / Esc](#)
[Printer-friendly Version](#)
[Interactive Discussion](#)

Table A2. Dissolved inorganic carbon (DIC), total alkalinity (TA), $\delta^{13}\text{C}$ -DIC, and $\Delta^{14}\text{C}$ -DIC in model boxes (concentrations in μM , isotope data in ‰): model vs. data.

Box	DIC data ^a	DIC model	TA data	TA model	$\delta^{13}\text{C}$ data ^b	$\delta^{13}\text{C}$ model	$\Delta^{14}\text{C}$ data ^a	$\Delta^{14}\text{C}$ model
NA _S	2074	2056	2410.0	2410	1.47	2.77	-75.6	-69.02
TA _S	2061	2032	2444.0	2453	1.64	2.77	-67.3	-65.35
SO _S	2104	2083	2365.0	2340	1.41	1.8	-85.1	-78.38
TIP _S	2006	1944	2359.0	2347	1.28	2.24	-60.1	-64.04
NP _S	2037	2022	2300.0	2306	1.3	2.27	-75.7	-72.01
AR _S	2101	2166	2372.0	2357	n. d.	2.11	n. d.	-68.26
NA _I	2179	2180	2391.0	2392	0.9	1.45	-75.0	-90.32
TA _I	2225	2259	2386.0	2400	0.84	0.625	-101.8	-114
SO _I	2254	2257	2392.0	2380	0.72	-0.053	-130.4	-126.5
TIP _I	2317	2311	2418.0	2391	0.32	-0.653	-148.3	-134.7
NP _I	2370	2373	2421.0	2436	-0.23	-0.875	-179.7	-183.3
AR _I	2169	2176	2373.0	2375	n. d.	1.79	n. d.	-78.03
NA _D	2216	2195	2388.0	2384	0.97	1.44	-87.9	-93.75
TA _D	2242	2239	2402.0	2401	0.96	0.933	-116.6	-122.3
SO _D	2315	2314	2431.0	2441	0.1	0.119	-166.0	-167.1
TIP _D	2382	2382	2481.0	2493	-0.06	-0.272	-199.6	-192.5
NP _D	2416	2388	2491.0	2492	-1.09	-0.432	-217.8	-214.2
AR _D	2188	2185	2371.0	2379	n. d.	1.62	n. d.	-85.97
NA _B	2241	2221	2403.0	2395	0.92	1.17	-118.4	-110.7
TA _B	2268	2253	2418.0	2411	0.77	0.792	-132.1	-132.9
SO _B	2318	2319	2434.0	2446	0.1	0.102	-162.7	-169.2
TIP _B	2360	2363	2472.0	2488	0.14	-0.111	-184.4	-184.7
NP _B	2388	2384	2491.0	2495	-0.58	-0.352	-206.8	-212.7
AR _B	2188	2186	2371.0	2379	n. d.	1.6	n. d.	-86.2

^a Corrected for anthropogenic CO_2 ; ^b not corrected for anthropogenic CO_2 ; n.d. = not determined.

Table A3. Water fluxes (in Sv) derived from the NEMO model run and fluxes applied in the box model to reproduce observed tracer distributions (Tables A1 and A2).

Fluxes NEMO	NEMO Net	NEMO Exchange	Fluxes Box model	Box model Net	Box model Exchange
NA _S → AR _S	1.1	2.64	NA _S → AR _S	3.0	1.74
NA _S → NA _I	0.43	12.2	NA _S → NA _I	9.93	42.2
TA _S → NA _S	1.48	7.26	TA _S → NA _S	12.83	0.36
SO _S → TA _S	1.34	4.33	SO _S → TA _S	12.94	0.43
SO _S → SO _I	10.43	77.58	SO _S → SO _I	3.93	106.58
TIP _S → SO _S	8.16	12.42	TIP _S → SO _S	15.94	12.42
NP _S → TIP _S	0.43	10.93	NP _S → TIP _S	0.31	2.93
NP _S → AR _S	1.14	0.03	NP _S → AR _S	1.14	0.03
AR _S → AR _I	2.37	10.38	AR _S → AR _I	4.37	45.38
NA _I → AR _I	2.11	24.51	NA _I → AR _I	2.11	14.51
NA _I → NA _D	2.23	23.08	NA _I → NA _D	8.23	0.08
TA _I → TA _S	0.58	24.91	TA _I → TA _S	0.58	0.41
TA _I → NA _I	3.91	27.73	TA _I → NA _I	0.41	17.73
SO _I → TA _I	3.42	24.89	TA _I → SO _I	0.08	4.87
SO _I → TIP _I	1.29	88.37	SO _I → TIP _I	13.79	73.37
TIP _I → TIP _S	11.39	77.11	TIP _I → TIP _S	16.39	77.11
NP _I → NP _S	1.26	16.98	NP _I → NP _S	1.26	3.98
NP _I → TIP _I	2.0	38.55	NP _I → TIP _I	2.0	3.55
AR _I → AR _D	4.48	6.87	AR _I → AR _D	6.48	6.87
NA _D → TA _D	10.35	3.89	NA _D → TA _D	15.35	1.19
TA _D → TA _I	1.07	13.78	TA _D → TA _I	1.07	8.78
TA _D → SO _D	9.29	5.68	TA _D → SO _D	15.29	1.68
SO _D → SO _D	5.72	224.4	SO _D → SO _I	9.78	10.12
SO _D → SO _B	19.65	84.24	SO _D → SO _B	17.65	114.24
TIP _D → TIP _I	8.1	18.08	TIP _D → TIP _I	0.6	3.08
TIP _D → SO _D	4.64	12.54	TIP _D → SO _D	12.14	2.54
NP _D → TIP _D	5.71	10.96	TIP _D → NP _D	1.29	0.67
NP _D → NP _I	3.26	2.48	NP _D → NP _I	3.26	1.48
AR _D → NA _D	4.48	1.0	AR _D → NA _D	6.48	11.
NA _B → NA _D	3.64	2.53	NA _B → NA _D	0.64	2.53
TA _B → TA _D	0.01	20.75	TA _B → TA _D	1.01	20.75
TA _B → NA _B	3.64	2.93	TA _B → NA _B	0.64	0.43
SO _B → TA _B	3.65	2.53	SO _B → TA _B	1.65	2.53
SO _B → TIP _B	16.0	0.72	SO _B → TIP _B	16.0	15.72
TIP _B → TIP _D	7.03	55.76	TIP _B → TIP _D	14.03	35.76
TIP _B → NP _B	8.97	8.65	TIP _B → NP _B	1.97	0.65
NP _B → NP _D	8.97	7.32	NP _B → NP _D	1.97	7.32
AR _B → AR _D	0	0.19	AR _B → AR _D	0	1.19
FRESH → NA _S	0.05		FRESH → NA _S	0.10	
FRESH → TA _S	-0.44		FRESH → TA _S	-0.69	
FRESH → SO _S	3.61		FRESH → SO _S	0.93	
FRESH → TIP _S	-3.66		FRESH → TIP _S	-0.76	
FRESH → NP _S	0.31		FRESH → NP _S	0.19	
FRESH → AR _S	0.13		FRESH → AR _S	0.23	

Effects of eustatic sea-level change, ocean dynamics, and iron fertilization on atmospheric $p\text{CO}_2$

K. Wallmann et al.

[Title Page](#)

[Abstract](#) [Introduction](#)

[Conclusions](#) [References](#)

[Tables](#) [Figures](#)

[◀](#) [▶](#)

[◀](#) [▶](#)

[Back](#) [Close](#)

[Full Screen / Esc](#)

[Printer-friendly Version](#)

[Interactive Discussion](#)



Effects of eustatic sea-level change, ocean dynamics, and iron fertilization on atmospheric $p\text{CO}_2$

K. Wallmann et al.

Table A4. Biogeochemical parameter values determined by fitting the model to observations.

Parameter	Symbol	Units	AR	NA	TA	SO	TIP	NP
Kinetic constant for export production	k_{EXP}	yr^{-1}	0.05	1.5	0.4	0.15	1.1	0.12
Kinetic constant for nitrogen fixation	k_{NF}	yr^{-1}	0.0	3.0	1.0	0.2	1.0	0.5
PIC/POC export ratio	r_{PICPOC}		0.01	0.08	0.20	0.01	0.15	0.07
Piston velocity	k_{SA}	cm yr^{-1}	0.4	0.1	0.12	0.12	0.24	0.1

[Title Page](#)
[Abstract](#)
[Introduction](#)
[Conclusions](#)
[References](#)
[Tables](#)
[Figures](#)
[Back](#)
[Close](#)
[Full Screen / Esc](#)
[Printer-friendly Version](#)
[Interactive Discussion](#)

Effects of eustatic sea-level change, ocean dynamics, and iron fertilization on atmospheric $p\text{CO}_2$

K. Wallmann et al.

[Title Page](#)[Abstract](#)[Introduction](#)[Conclusions](#)[References](#)[Tables](#)[Figures](#)[⏪](#)[⏩](#)[◀](#)[▶](#)[Back](#)[Close](#)[Full Screen / Esc](#)[Printer-friendly Version](#)[Interactive Discussion](#)**Table A5.** Difference in $\delta^{13}\text{C}$ -DIC between LGM (21 ka) and Holocene (5 ka) as derived from data (Oliver et al., 2010; Sarnthein et al., 1994) and calculated in the standard model run.

Box	Data	Model
NA _I	+0.04 ± 0.28	+0.01
NA _D	-0.55 ± 0.16	-0.60
NA _B	-0.70 ± 0.13	-0.70
TA _I	+0.15 ± 0.20	+0.22
TA _D	-0.55 ± 0.24	-0.66
TA _B	-0.78 ± 0.21	-0.73
SO _D	-0.44 ± 0.26	-0.52
TIP _D	-0.44 ± 0.20	-0.36

Effects of eustatic sea-level change, ocean dynamics, and iron fertilization on atmospheric $p\text{CO}_2$

K. Wallmann et al.

Table B1. Parameter values applied in the simulation of margin processes.

Parameter	Symbol	Value	Source
Modern seafloor area at 0–50 m	A_{NM}	$13.54 \times 10^6 \text{ km}^2$	Eakins and Sharman (2012)
Modern seafloor area at 0–100 m	A_{SM}	$20.34 \times 10^6 \text{ km}^2$	Eakins and Sharman (2012)
Modern seafloor area at 100–2000 m	A_{IM}	$38.29 \times 10^6 \text{ km}^2$	Eakins and Sharman (2012)
Modern rate of neritic carbonate burial	F_{BPICSM}	10 Tmol yr^{-1}	Kleypas (1997)
Modern rate of marine POC burial at 0–100 m	F_{BPOCSM}	5 Tmol yr^{-1}	Wallmann et al. (2012)
Modern rate of marine POC burial at 100–2000 m	F_{BPOCIM}	5 Tmol yr^{-1}	Wallmann et al. (2012)
Modern rate of marine POC burial at 2000–4000 m	F_{BPOCDM}	1.3 Tmol yr^{-1}	Wallmann et al. (2012)
Modern rate of marine POC burial at > 4000 m	F_{BPOCBM}	0.2 Tmol yr^{-1}	Wallmann et al. (2012)
Modern POC export production	F_{EPOCM}	809 Tmol yr^{-1}	Sarmiento and Gruber (2006)
Modern rate of marine P burial at 0–100 m	F_{BPSM}	$0.05 \text{ Tmol yr}^{-1}$	Wallmann (2010)
Modern rate of marine P burial at 100–2000 m	F_{BPIM}	$0.05 \text{ Tmol yr}^{-1}$	Wallmann (2010)
Modern rate of marine P burial at 2000–4000 m	F_{BPDm}	$0.06 \text{ Tmol yr}^{-1}$	Wallmann (2010)
Modern rate of marine P burial at > 4000 m	F_{BPBM}	$0.02 \text{ Tmol yr}^{-1}$	Wallmann (2010)
Monod constant for P burial	k_{P}	$20 \mu\text{M}$	Wallmann (2010)
Burial efficiency of marine POC at 0–100 m	BE_{S}	0.05	This work
Burial efficiency of marine POC at 100–2000 m	BE_{I}	0.2	This work
Burial efficiency of marine POC at 2000–4000 m	BE_{D}	0.1	This work
Burial efficiency of marine POC at > 4000 m	BE_{B}	0.02	This work

Title Page

Abstract

Introduction

Conclusions

References

Tables

Figures

◀

▶

◀

▶

Back

Close

Full Screen / Esc

Printer-friendly Version

Interactive Discussion



Effects of eustatic sea-level change, ocean dynamics, and iron fertilization on atmospheric $p\text{CO}_2$

K. Wallmann et al.

Table B2. Flux parameterizations applied in the simulation of margin processes.

Process	Equation*
Neritic carbonate burial	$F_{\text{BPICS}} = F_{\text{BPICSM}} \cdot \frac{A_{\text{N}}}{A_{\text{NM}}}$
POC burial at 0–100 m	$F_{\text{BPOCS}} = F_{\text{BPOCSM}} \cdot \frac{F_{\text{EPOC}}}{F_{\text{EPOCM}}} \cdot \frac{A_{\text{S}}}{A_{\text{SM}}}$
POC burial at 100–2000 m	$F_{\text{BPOCI}} = F_{\text{BPOCIM}} \cdot \frac{F_{\text{EPOC}}}{F_{\text{EPOCM}}} \cdot \frac{A_{\text{I}}}{A_{\text{IM}}}$
POC burial at 2000–4000 m	$F_{\text{BPOCD}} = F_{\text{BPOCDM}} \cdot \frac{F_{\text{EPOC}}}{F_{\text{EPOCM}}} \cdot \frac{A_{\text{SM}} + A_{\text{IM}}}{A_{\text{S}} + A_{\text{I}}}$
POC burial at > 4000 m	$F_{\text{BPOCB}} = F_{\text{BPOCBM}} \cdot \frac{F_{\text{EPOC}}}{F_{\text{EPOCM}}} \cdot \frac{A_{\text{SM}} + A_{\text{IM}}}{A_{\text{S}} + A_{\text{I}}}$
P burial at 0–100 m	$F_{\text{BPS}} = F_{\text{BPMS}} \cdot \frac{F_{\text{EPOC}}}{F_{\text{EPOCM}}} \cdot \frac{A_{\text{S}}}{A_{\text{SM}}} \cdot \frac{\text{DO}_{\text{S}}}{\text{DO}_{\text{S}} + k_{\text{P}}} \cdot \frac{\text{DO}_{\text{SM}} + k_{\text{P}}}{\text{DO}_{\text{SM}}}$
P burial at 100–2000 m	$F_{\text{BPI}} = F_{\text{BPIM}} \cdot \frac{F_{\text{EPOC}}}{F_{\text{EPOCM}}} \cdot \frac{A_{\text{I}}}{A_{\text{IM}}} \cdot \frac{\text{DO}_{\text{I}}}{\text{DO}_{\text{I}} + k_{\text{P}}} \cdot \frac{\text{DO}_{\text{IM}} + k_{\text{P}}}{\text{DO}_{\text{IM}}}$
P burial at 2000–4000 m	$F_{\text{BPD}} = F_{\text{BPDM}} \cdot \frac{F_{\text{EPOC}}}{F_{\text{EPOCM}}} \cdot \frac{\text{DO}_{\text{D}}}{\text{DO}_{\text{D}} + k_{\text{P}}} \cdot \frac{\text{DO}_{\text{DM}} + k_{\text{P}}}{\text{DO}_{\text{DM}}}$
P burial at > 4000 m	$F_{\text{BPB}} = F_{\text{BPBM}} \cdot \frac{F_{\text{EPOC}}}{F_{\text{EPOCM}}} \cdot \frac{\text{DO}_{\text{B}}}{\text{DO}_{\text{B}} + k_{\text{P}}} \cdot \frac{\text{DO}_{\text{BM}} + k_{\text{P}}}{\text{DO}_{\text{BM}}}$
Benthic denitrification with $i = (\text{S}, \text{I}, \text{D}, \text{B})$	$F_{\text{BDEN}_i} = \frac{F_{\text{BPOCI}}}{\text{BE}_i} \cdot (0.06 + 0.19 \cdot 0.99^{(\text{DO}_i - \text{DN}_i)})$

* Subscripts indicate modern values (M) and the following environments: shelf (S, 0–100 m water depth), outer shelf and slope (I, 100–2000 m), continental rise and deep-sea floor (D, 2000–4000 m), deep-sea floor and abyssal plain (B, > 4000 m). The equations define global fluxes. These were distributed among the ocean basins considered their export production and the seafloor areas of individual boxes.

Title Page

Abstract

Introduction

Conclusions

References

Tables

Figures

◀

▶

◀

▶

Back

Close

Full Screen / Esc

Printer-friendly Version

Interactive Discussion



Effects of eustatic sea-level change, ocean dynamics, and iron fertilization on atmospheric $p\text{CO}_2$

K. Wallmann et al.

Table C2. Effect of radiocarbon production rate on atmospheric and marine ^{14}C values under steady-state conditions. $R_{14}(0)$ is the pre-human atmospheric production rate applied in the model calibration ($1.64 \text{ atoms cm}^{-2} \text{ s}^{-1} = 437 \text{ mol yr}^{-1}$).

Rate	$\Delta^{14}\text{C-CO}_2$ (‰)	$\Delta^{14}\text{C-DIC}$ (‰)	$\Delta\Delta^{14}\text{C-DIC}$ (‰)
$R_{14}(0)$	+0	−148	−148
$1.5 \times R_{14}(0)$	+500	+278	−222
$2.0 \times R_{14}(0)$	+1000	+704	−296

[Title Page](#)
[Abstract](#)
[Introduction](#)
[Conclusions](#)
[References](#)
[Tables](#)
[Figures](#)
[Back](#)
[Close](#)
[Full Screen / Esc](#)
[Printer-friendly Version](#)
[Interactive Discussion](#)

Table C3. $\Delta\Delta^{14}\text{C}$ -DIC for the LGM (19–23 ka) calculated in simulation STD and derived from radiocarbon measurements in foraminifera (atmosphere – water differences).

Box	Model	Data	Reference
AR _s	–196 to –177	EAST: –95 to –60 WEST: –210 to –240	GIK 23074 (66°66.67' N, 4°90' E, 1157 m, Norw. Current) Sarnthein et al. (2015) PS2644 (67°52.02' N, 21°45.92' W, 777 m, East Greenland Current) Sarnthein et al. (2013, 2015)
AR _i	–206 to –187	–50 –220 to –270	PS2644 (67°52.02' N, 21°45.92' W, 777 m, millennial-scale oscillations?) Sarnthein et al. (2013)
NA _s	–169 to –153	–115 to –40	MD90–917 (41°29.78' N, 17°61.3' E, 1010 m) MD99-2334K (37°48' N, 10°10' W, 3146 m) RAPID-17-5P (61°29' N, 19°32' W, 2303 m) Thornalley et al. (2011) MD08-3180 (38° N, 31°13.45' W, 3064 m) Sarnthein et al. (2013)
NA _D	–257 to –228	–40 to –60 –260 to –275	MD99-2334K (37°48' N, 10°10' W, 3146 m) RAPID-17-5P (61°29' N, 19°32' W, 2303 m) Thornalley et al. (2011) MD08-3180 (38° N, 31°13.45' W, 3064 m) Sarnthein et al. (2015)
NA _B	–285 to –253	–330	Extrapolated from Portuguese margin site MD99-2334K (37°48' N, 10°10' W, 3146 m, a site subject to enhanced Coriolis forcing) Skinner et al. (2014) and assuming a transit time of ~ 800 yr from TNO57-21 (41°06' S, 7°48' E, 4981 m) Barker et al. (2010)
TA _s	–128 to –108	–130 to –95	ODP 1002 (10°42.37' N, 65°10.18' W, 893 m) and southward extrapolated from MD08-3180 (38° N, 31°13.45' W, 3064 m) Sarnthein et al. (2015)
TA _i	–241 to –218	–160 to –185 –85	Dredged coral transects at Gregg, Manning, and Muir Sea Mt. 33–39° N, < 2300 m, corr. according to Robinson et al. (2005)
SO _s	–160 to –140	–270 to –190	MD07-3076 (44°09' S, 14°13' W, 3770 m) Skinner et al. (2010)
SO _i	–228 to –201	–220 to –210	Dredged coral transect Drake Passage, < 1800 m Burke et al. (1982), + AWI unpubl. data under review
SO _D	–332 to –296	–300 to –185 –600 to –500	D07-3076 (44°09' S, 14°13' W, 3770 m) ATL. SECTOR: Skinner et al. (2010) Sonne core transect off New Zealand PAC. SECTOR: AWI unpubl. records, under review
SO _B	–335 to –299	–230 to –130	TNO57-21 (41°06' S, 7°48' E, 4981 m) Barker et al. (2010)
TIP _s	–139 to –120	–220 to –105	MD01-2378 (13°08.25' S, 121°78.8' E, 1783 m) Sarnthein et al. (2015)
TIP _i	–238 to –211	–264 to –61 –205 to –190 –220 to –165	RC 27-14 (18.3° N, 57.6° E, 596 m) RC 27-23 (18.0° N, 57.6° E, 820 m) Bryan et al. (2010) MD01-2378 (13°08.25' S, 121°78.8' E, 1783 m) Sarnthein et al. (2013)
TIP _D	–363 to –324	–410 to –320	MD01-2378 (13°08.25' S, 121°78.8' E, 1783 m) GIK 17940 (20°07.0' N, 117°23.0' E, 1727 m) extrapolated to > 2000 m Sarnthein et al. (2013)
NP _s	–156 to –137	–190 to –115	MD01-2416 (51°26.8' N, 167°72.5' E, 2317 m) MD02-2489 (54°39.07' N, 148°92.13' W, 3640 m) Sarnthein et al. (2013, 2015)
NP _D	–378 to –337	–470	MD01-2416 (51°26.8' N, 167°72.5' E, 2317 m) Sarnthein et al. (2013, 2015)
NP _B	–375 to –335	–270	MD02-2489 (54°39.07' N, 148°92.13' W, 3640 m) extrapolated to > 4000 m Sarnthein et al. (2013; Gebhardt et al., 2008)

Effects of eustatic sea-level change, ocean dynamics, and iron fertilization on atmospheric $p\text{CO}_2$

K. Wallmann et al.

Title Page

Abstract

Introduction

Conclusions

References

Tables

Figures



Back

Close

Full Screen / Esc

Printer-friendly Version

Interactive Discussion



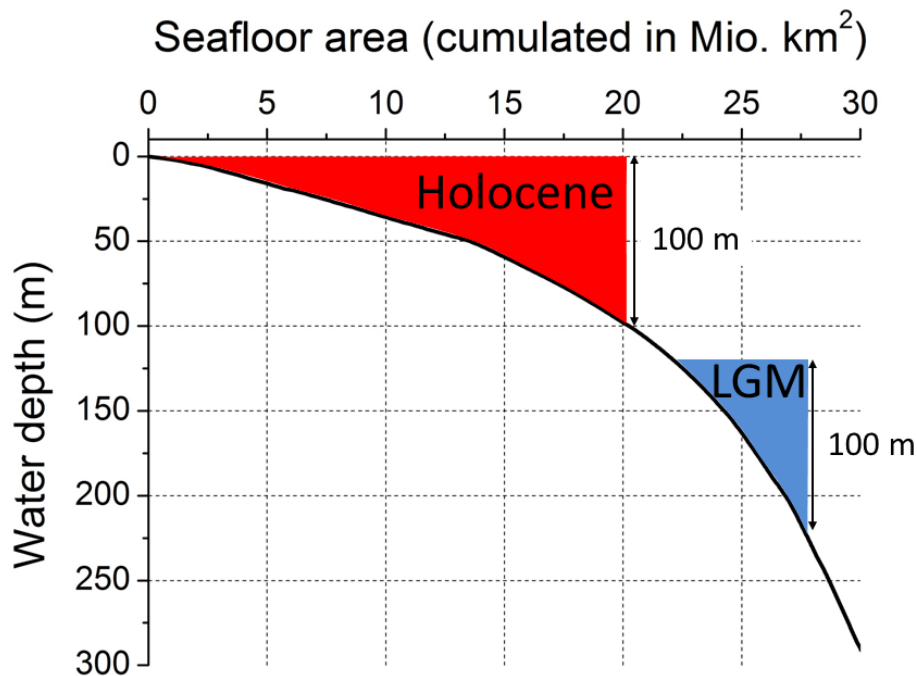


Figure 1. Morphology of global ocean margin. The black line is the cumulated seafloor area as derived from the high-resolution ETOPE 1 grid (Eakins and Sharman, 2012). The ocean margin at 0–100 m water depth is indicated for the modern ocean (red area) and for the LGM when eustatic sea-level was lowered by 120 m (blue area). The global ocean retreated into steeper terrain during the glacial marine regression. The seafloor areas covered by shallow waters were reduced by this steepening of ocean margins.

Effects of eustatic sea-level change, ocean dynamics, and iron fertilization on atmospheric $p\text{CO}_2$

K. Wallmann et al.

[Title Page](#)

[Abstract](#) | [Introduction](#)

[Conclusions](#) | [References](#)

[Tables](#) | [Figures](#)

[◀](#) | [▶](#)

[◀](#) | [▶](#)

[Back](#) | [Close](#)

[Full Screen / Esc](#)

[Printer-friendly Version](#)

[Interactive Discussion](#)



Effects of eustatic sea-level change, ocean dynamics, and iron fertilization on atmospheric $p\text{CO}_2$

K. Wallmann et al.

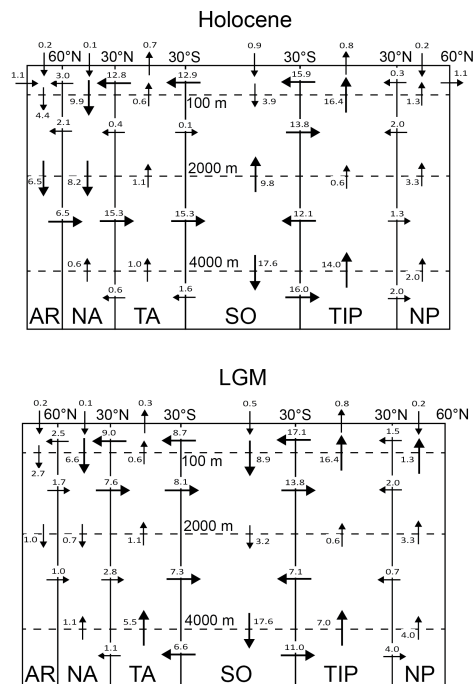


Figure 2. Set-up of the box model: the global ocean is separated into 24 boxes representing surface (0–100 m), intermediate (100–2000 m), deep (2000–4000 m), and bottom (> 4000 m) waters in the Arctic (AR), North Atlantic (NA), Tropical Atlantic (TA), Southern Ocean (SO), Tropical Indo-Pacific (TIP), and North Pacific (NP). Arrows with numbers indicate net water fluxes between boxes in Sv; major fluxes (> 5 Sv) are represented by large arrows, minor fluxes (< 5 Sv) by small arrows. Arrows crossing the top boundary of the surface water boxes (seawater–atmosphere interface) indicate net freshwater fluxes (precipitation + river water fluxes – evaporation). The upper panel shows the circulation field applied for the modern ocean and the previous interglacial, the lower panel shows the circulation applied over the LGM.

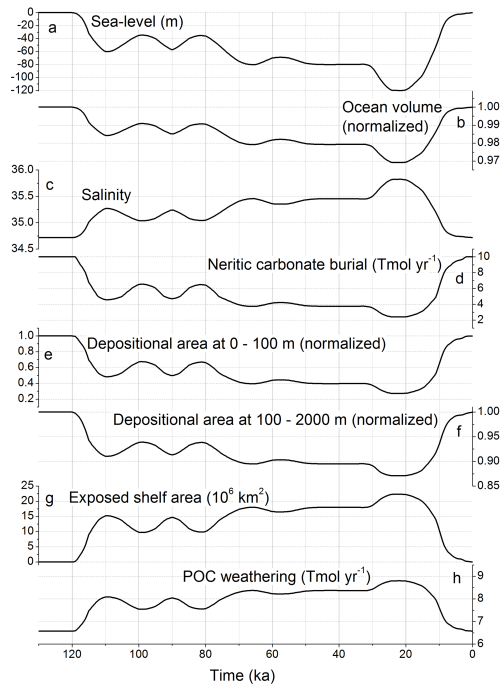


Figure 3. Model forcing related to sea-level change. **(a)** Eustatic sea-level (Waelbroeck et al., 2002; Stanford et al., 2011); **(b)** global ocean volume as calculated from eustatic sea-level and ocean bathymetry data (Eakins and Sharman, 2012); **(c)** salinity of global mean seawater as calculated from global ocean volume; **(d)** global burial rate of neritic carbonate as calculated from seafloor area at 0–50 m water depth (Kleypas, 1997; Wallmann, 2014); **(e–f)** seafloor area at 0–100 and 100–2000 m water depth calculated from sea-level and ocean bathymetry data (Eakins and Sharman, 2012); **(g)** exposed shelf area calculated from sea-level and ocean bathymetry data (Eakins and Sharman, 2012); **(h)** global rate of POC weathering calculated from exposed shelf area (Wallmann, 2014).

Effects of eustatic sea-level change, ocean dynamics, and iron fertilization on atmospheric $p\text{CO}_2$

K. Wallmann et al.

[Title Page](#)

[Abstract](#) | [Introduction](#)

[Conclusions](#) | [References](#)

[Tables](#) | [Figures](#)

[◀](#) | [▶](#)

[◀](#) | [▶](#)

[Back](#) | [Close](#)

[Full Screen / Esc](#)

[Printer-friendly Version](#)

[Interactive Discussion](#)



Effects of eustatic sea-level change, ocean dynamics, and iron fertilization on atmospheric $p\text{CO}_2$

K. Wallmann et al.

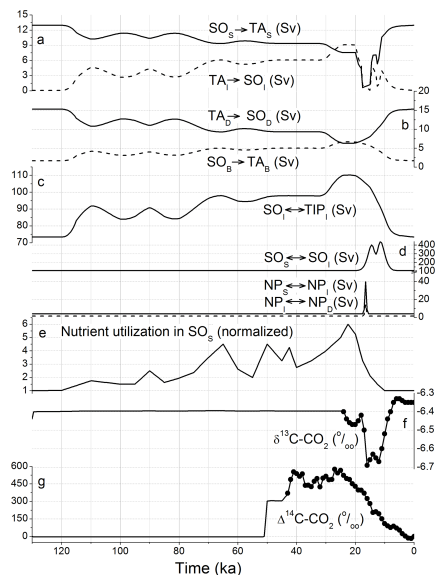


Figure 4. Model forcing applied to define ocean circulation, nutrient utilization in the Southern Ocean, and the isotopic composition of atmospheric CO_2 . **(a–b)** Net water fluxes between Southern Ocean (SO) and Tropical Atlantic (TA). The horizontal flows are given for (from top to bottom) surface water (subscript S), intermediate water (subscript I), deep water (subscript D), and bottom water (subscript B); **(c)** horizontal exchange flux between Southern Ocean and Tropical Indo-Pacific intermediate waters; **(d)** vertical water exchange fluxes in the Southern Ocean and North Pacific across 100 m water depth (solid lines) and 2000 m water depth (broken line); **(e)** nutrient utilization in the Southern Ocean (Martinez-Garcia et al., 2014); **(f)** $\delta^{13}\text{C}$ value of atmospheric CO_2 . Dots indicate ice-core data (Schmitt et al., 2012) while the solid line defines the values applied in the model. For > 24 ka, where data are not available, the $\delta^{13}\text{C}$ - CO_2 value is set to -6.4% ; **(g)** $\Delta^{14}\text{C}$ value of atmospheric CO_2 , dots indicate values reconstructed from the geological record (Reimer et al., 2013) while the solid line defines the values applied in the model. For > 50 ka, where data are not available, the atmospheric $\Delta^{14}\text{C}$ - CO_2 is assumed to correspond to the pre-anthropogenic modern value (0%).

Effects of eustatic sea-level change, ocean dynamics, and iron fertilization on atmospheric $p\text{CO}_2$

K. Wallmann et al.

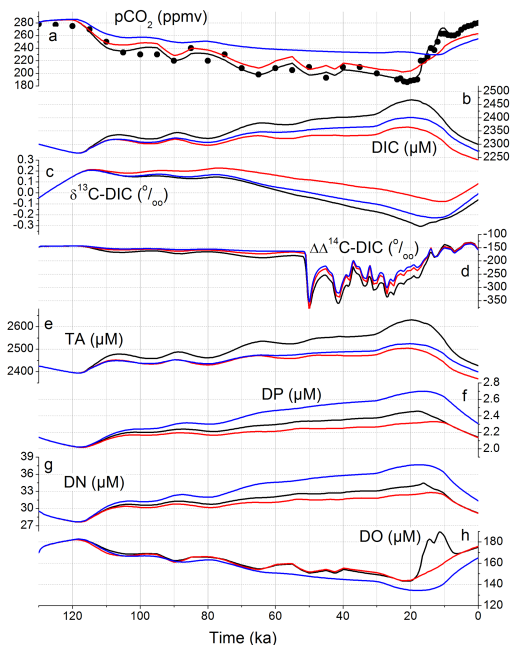


Figure 5. Model results for the standard case (simulation STD, black lines), for constant circulation (simulation STD-CC, red lines), and constant circulation and nutrient utilization (simulation STD-CC-CN, blues lines). **(a)** Atmospheric $p\text{CO}_2$, dots indicate ice core data (Monnin et al., 2001; Petit et al., 1999; Monnin et al., 2004); **(b–h)** global mean seawater concentrations and isotopic compositions; **(b)** dissolved inorganic carbon (DIC); **(c)** $\delta^{13}\text{C}$ of DIC; **(d)** difference between radiocarbon in seawater DIC and atmospheric CO_2 ($\Delta\Delta^{14}\text{C-DIC} = \Delta^{14}\text{C-DIC} - \Delta^{14}\text{C-CO}_2$); **(e)** total alkalinity (TA); **(f)** dissolved phosphorus (DP); **(g)** dissolved reactive nitrogen (DN); **(h)** dissolved oxygen (DO).

[Title Page](#)
[Abstract](#)
[Introduction](#)
[Conclusions](#)
[References](#)
[Tables](#)
[Figures](#)
[◀](#)
[▶](#)
[◀](#)
[▶](#)
[Back](#)
[Close](#)
[Full Screen / Esc](#)
[Printer-friendly Version](#)
[Interactive Discussion](#)

Effects of eustatic sea-level change, ocean dynamics, and iron fertilization on atmospheric $p\text{CO}_2$

K. Wallmann et al.

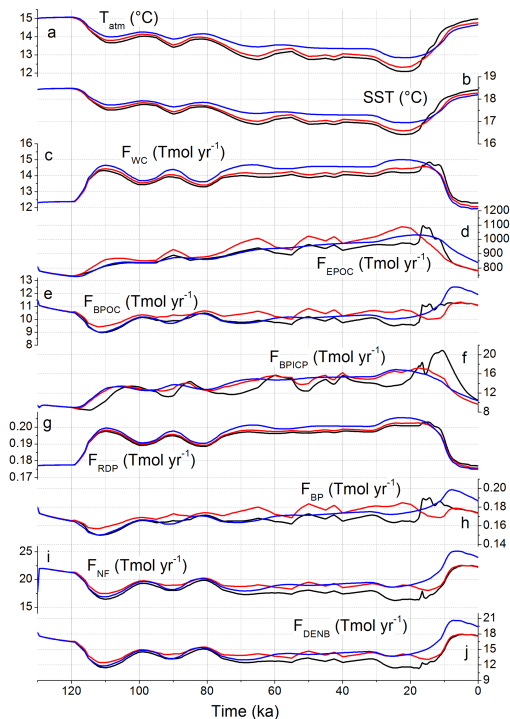


Figure 6. Model results for simulations STD (black lines), STD-CC (red lines), and STD-CC-CN (blue lines). **(a)** Global mean atmospheric near-surface temperature (T_{atm}); **(b)** global mean sea surface temperature (SST); **(c–j)** global rates; **(c)** carbonate weathering (F_{WC}); **(d)** marine export production of POC (F_{EPOC}); **(e)** POC burial (F_{BPPOC}); **(f)** burial of pelagic carbonate (F_{BPICP}); **(g)** riverine flux of dissolved phosphorus (F_{RDP}); **(h)** burial of marine phosphorus (F_{BP}); **(i)** nitrogen fixation (F_{NF}); **(j)** benthic denitrification (F_{DENB}).

Title Page

Abstract

Introduction

Conclusions

References

Tables

Figures

◀

▶

◀

▶

Back

Close

Full Screen / Esc

Printer-friendly Version

Interactive Discussion

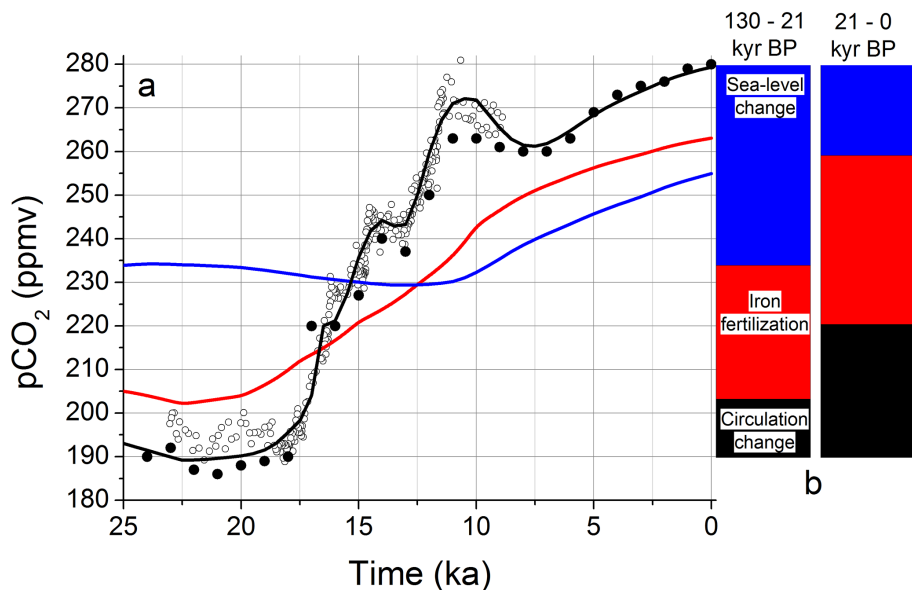


Figure 7. Atmospheric $p\text{CO}_2$ over the last 25 kyr. **(a)** Model results for simulations STD (black line), STD-CC (red line), and STD-CC-CN (blue line); solid dots indicate ice core data by (Monnin et al., 2001, 2004) while ice core data reported in (Marcott et al., 2014) are shown as open circles; **(b)** relative contribution of sea-level change (blue), iron fertilization (red), and ocean circulation changes (black) to $p\text{CO}_2$ model results; the left hand column shows contributions to the glacial $p\text{CO}_2$ draw-down (51 % induced by sea-level fall, 34 % by enhanced iron fertilization, 15 % by changes in ocean circulation); the right hand column indicates the driving forces for the deglacial $p\text{CO}_2$ rise (23 % induced by sea-level rise, 43 % by decrease in iron fertilization, 34 % by changes in ocean circulation).

Effects of eustatic sea-level change, ocean dynamics, and iron fertilization on atmospheric $p\text{CO}_2$

K. Wallmann et al.

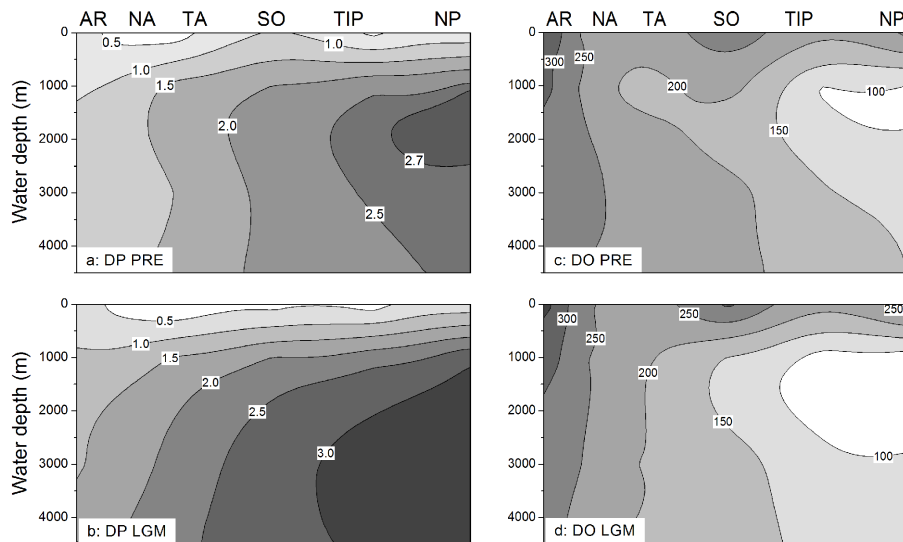


Figure 8. Concentrations (in μM) of dissolved phosphorus (DP) and oxygen (DO) in the pre-anthropogenic modern ocean (PRE, model results for 0 ka, **a**: DP, **c**: DO) and during the LGM (model results for 21 ka, **b**: DP, **d**: DO). The contour plots shown here and in the following figures are based on concentrations calculated in simulation STD for each of the 24 ocean boxes depicted in Fig. 2.

Title Page

Abstract

Introduction

Conclusions

References

Tables

Figures

◀

▶

◀

▶

Back

Close

Full Screen / Esc

Printer-friendly Version

Interactive Discussion

Effects of eustatic sea-level change, ocean dynamics, and iron fertilization on atmospheric $p\text{CO}_2$

K. Wallmann et al.

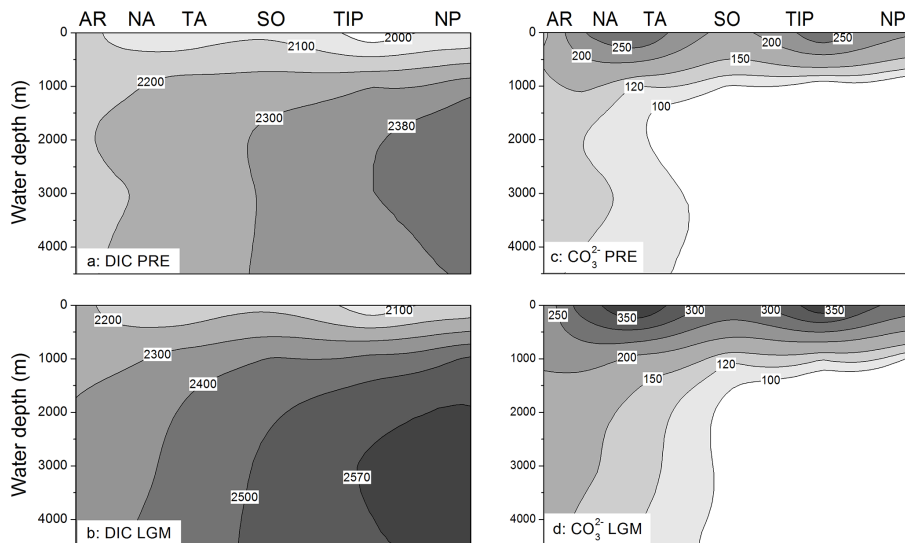


Figure 9. Concentrations of dissolved inorganic carbon (DIC in μM) and carbonate ions (CO_3^{2-} in $\mu\text{mol kg}^{-1}$) in the pre-anthropogenic modern ocean (PRE, model results for 0 ka, **a**: DIC, **c**: CO_3^{2-}) and during the LGM (model results for 21 ka, **b**: DIC, **d**: CO_3^{2-}). See legend of Fig. 8 for further information.

[Title Page](#)

[Abstract](#)

[Introduction](#)

[Conclusions](#)

[References](#)

[Tables](#)

[Figures](#)

[◀](#)

[▶](#)

[◀](#)

[▶](#)

[Back](#)

[Close](#)

[Full Screen / Esc](#)

[Printer-friendly Version](#)

[Interactive Discussion](#)

Effects of eustatic sea-level change, ocean dynamics, and iron fertilization on atmospheric $p\text{CO}_2$

K. Wallmann et al.

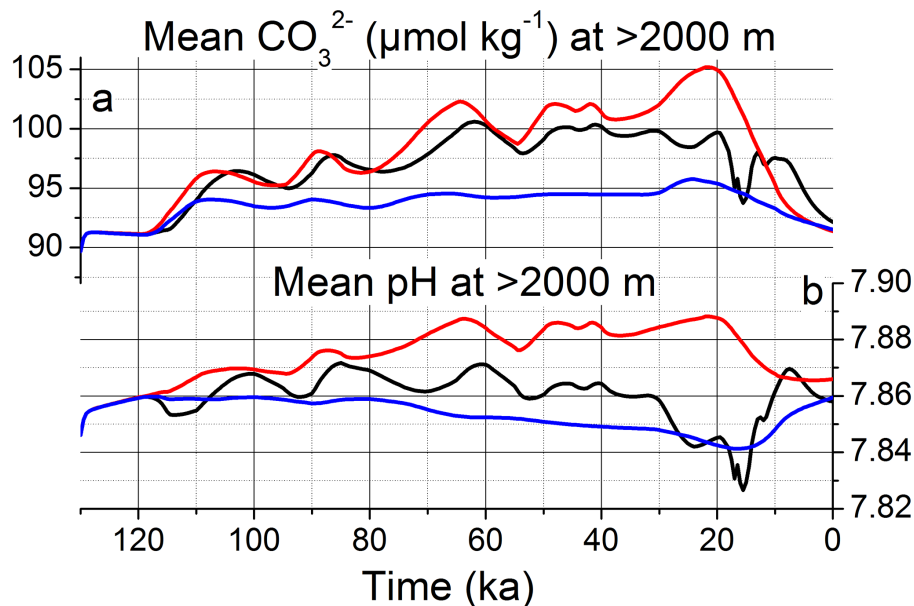


Figure 10. Global mean carbonate ion concentrations (a) and pH values (b) below 2000 m water depth for simulations STD (black line), STD-CC (red line), and STD-CC-CN (blue line).

Effects of eustatic sea-level change, ocean dynamics, and iron fertilization on atmospheric $p\text{CO}_2$

K. Wallmann et al.

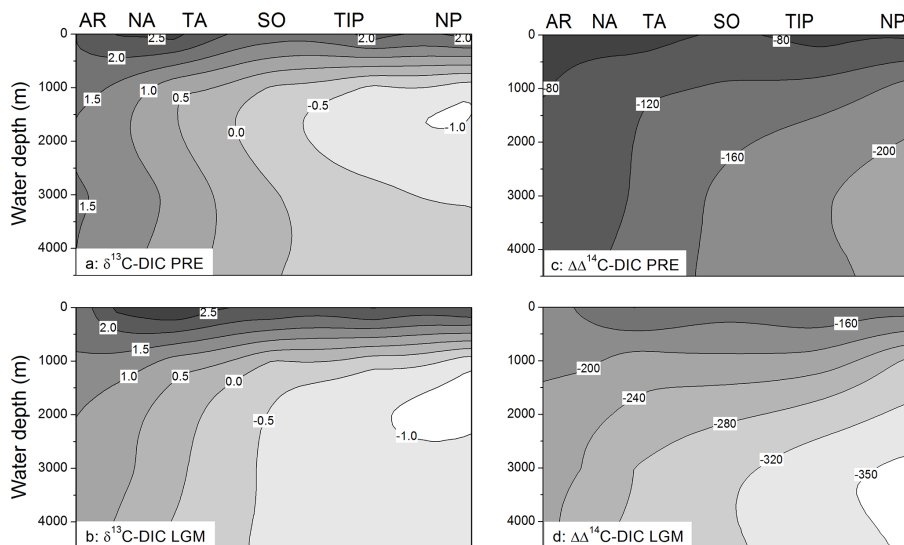


Figure 11. Isotopic composition of dissolved inorganic carbon (DIC) in the global ocean. $\delta^{13}\text{C}$ of dissolved inorganic carbon ($\delta^{13}\text{C-DIC}$ in ‰) and radiocarbon composition of dissolved inorganic carbon ($\Delta\Delta^{14}\text{C-DIC}$ in ‰) in the pre-anthropogenic modern ocean (PRE, model results for 0 ka, **a:** $\delta^{13}\text{C-DIC}$, **c:** $\Delta\Delta^{14}\text{C-DIC}$) and during the LGM (model results for 21 ka, **b:** $\delta^{13}\text{C-DIC}$, **d:** $\Delta\Delta^{14}\text{C-DIC}$). $\Delta\Delta^{14}\text{C-DIC}$ values represent the difference between the atmospheric value (0 ‰ for the pre-anthropogenic modern atmosphere, +446 ‰ for the LGM atmosphere) and seawater $\Delta^{14}\text{C-DIC}$. See legend of Fig. 8 for further information.

Title Page

Abstract

Introduction

Conclusions

References

Tables

Figures

◀

▶

◀

▶

Back

Close

Full Screen / Esc

Printer-friendly Version

Interactive Discussion

Effects of eustatic sea-level change, ocean dynamics, and iron fertilization on atmospheric $p\text{CO}_2$

K. Wallmann et al.

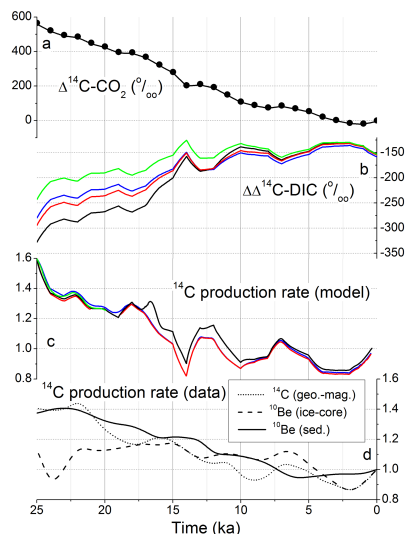


Figure 12. Radiocarbon values and production rates. **(a)** Atmospheric $\Delta^{14}\text{C-CO}_2$; dots are IntCal13 data (Reimer et al., 2013) while the black line shows the values applied in the model runs, **(b)** marine $\Delta\Delta^{14}\text{C-DIC}$ values calculated as difference between radiocarbon in seawater DIC and atmospheric CO_2 . The results of simulations STD-CC-CN, STD-CC, and STD are indicated as blue, red and black lines, respectively. The green line indicates the results obtained in a steady-state simulation under Holocene boundary conditions where all variables except atmospheric $\Delta^{14}\text{C-CO}_2$ and radiocarbon production rate were kept constant over time. **(c)** Production rates of radiocarbon in the atmosphere calculated in the model runs and normalized to the pre-anthropogenic modern value ($1.64 \text{ atoms cm}^2 \text{ s}^{-1}$); **(d)** ^{14}C production rates calculated from the geo-magnetic record (Laj et al., 2002), ^{10}Be production rate as reconstructed from Greenland ice core data (Muscheler et al., 2005; Reimer et al., 2013), ^{10}Be production rate as reconstructed from sediment data (Frank et al., 1997); all rates are normalized to their pre-anthropogenic modern values

[Title Page](#)
[Abstract](#)
[Introduction](#)
[Conclusions](#)
[References](#)
[Tables](#)
[Figures](#)
[◀](#)
[▶](#)
[◀](#)
[▶](#)
[Back](#)
[Close](#)
[Full Screen / Esc](#)
[Printer-friendly Version](#)
[Interactive Discussion](#)

Effects of eustatic sea-level change, ocean dynamics, and iron fertilization on atmospheric $p\text{CO}_2$

K. Wallmann et al.

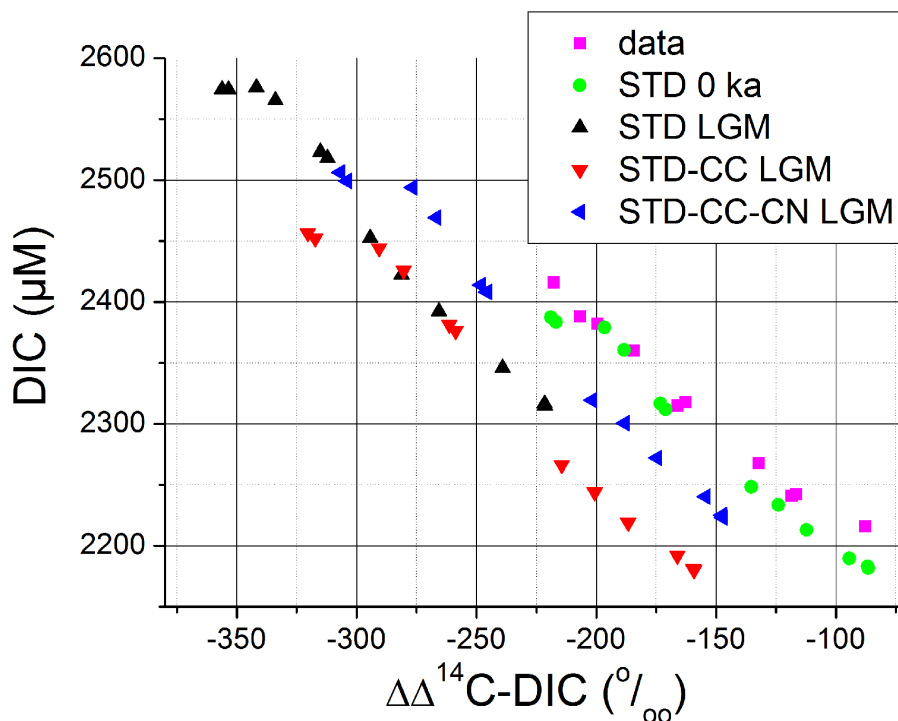


Figure 13. DIC vs. difference between radiocarbon in seawater DIC and atmospheric CO_2 ($\Delta\Delta^{14}\text{C-DIC}$) at $> 2000\text{ m}$ water depth. Data are mean values for deep water and bottom water boxes derived from water column measurements. Model results are shown for the standard case (STD), for constant circulation (STD-CC), and constant values for circulation and nutrient utilization (STD-CC-CN). LGM refers to model results at 21 ka.

[Title Page](#)
[Abstract](#)
[Introduction](#)
[Conclusions](#)
[References](#)
[Tables](#)
[Figures](#)
[◀](#)
[▶](#)
[◀](#)
[▶](#)
[Back](#)
[Close](#)
[Full Screen / Esc](#)
[Printer-friendly Version](#)
[Interactive Discussion](#)

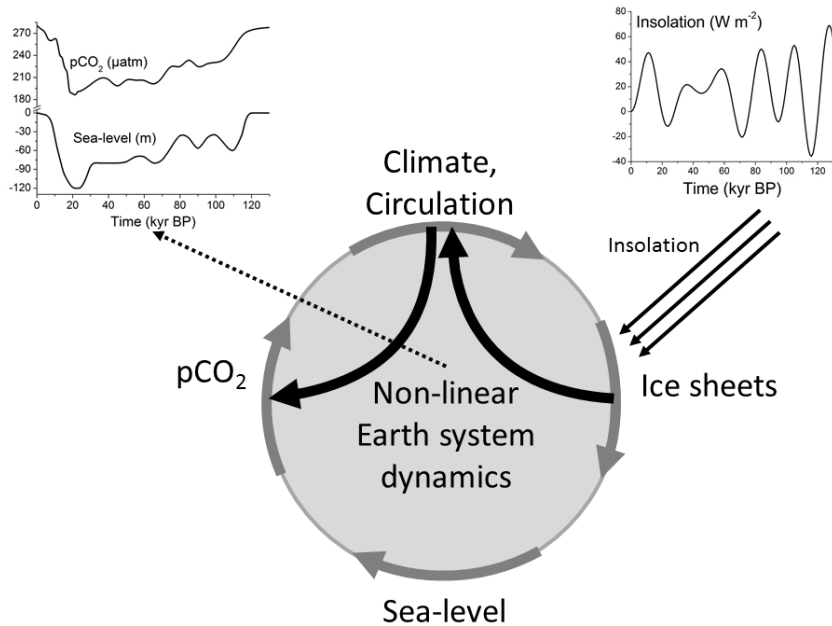


Figure 14. Key elements of the 100 kyr cycle. Summer insolation at high northern latitudes (June insolation at 60° N, diagram in the upper right corner, Berger and Loutre, 1991) affects the growth and melting of continental ice sheets and thereby eustatic sea-level change. The glacial draw-down of atmospheric $p\text{CO}_2$ and its deglacial rise are supported by sea-level change. The cycle is closed by atmospheric $p\text{CO}_2$ affecting global climate and thereby the volume of continental ice sheets. It is accelerated and further strengthened by additional positive feedbacks: Ice sheets affect the Earth's albedo and climate while changes in ocean and atmosphere circulation and dust deposition support the glacial $p\text{CO}_2$ draw-down and are largely responsible for the rapid deglacial rise in atmospheric $p\text{CO}_2$. The records of atmospheric $p\text{CO}_2$ and eustatic sea-level change (diagrams in the upper left corner, Monnin et al., 2001, 2004; Petit et al., 1999; Waelbroeck et al., 2002; Stanford et al., 2011) reflect the internal non-linear dynamics of the Earth system and its response to external insolation forcing.

Effects of eustatic sea-level change, ocean dynamics, and iron fertilization on atmospheric $p\text{CO}_2$

K. Wallmann et al.

Title Page

Abstract Introduction

Conclusions References

Tables Figures

◀ ▶

◀ ▶

Back Close

Full Screen / Esc

Printer-friendly Version

Interactive Discussion

